Application of the Convergence-Confinement Method of Tunnel Design to Rock Masses That Satisfy the Hoek-Brown Failure Criterion

C. Carranza-Torres and C. Fairhurst

Abstract *—This paper discusses the practical application of the Convergence-Confinement Method of tunnel design to rock-masses that satisfy the Hoek-Brown failure criterion. The strength of intact rock and jointed rock-masses, as defined by the Hoek-Brown criterion, and the basis of the Convergence-Confinement method are reviewed. Equations that allow the construction of the three basic components of the Convergence-Confinement method, i) the Longitudinal Deformation Profile (LDP), ii) the Ground Reaction Curve (GRC) and iii) the Support Characteristic Curve (SCC) are given. A practical case of support design for a circular tunnel is discussed and solved using the Convergence Confinement method. A spreadsheet summarizing the implementation of the method is also included. Reference values of typical rock properties and geometrical and mechanical properties for typical support systems are presented in tables and charts.*

1. Introduction

Estimation of the support required to stabilize a tunnel excavation, especially in the vicinity of the face, is essentially a four-dimensional problem. Time-dependent weakening of the rock compounds the three-dimensional redistribution of forces around the excavation, and the nature of the rock is uncertain until it is exposed in the face. Labasse (1949) describes the situation as follows:

> *First, the types of supports to be used must be limited to one or two in order not to disrupt the material supply operations underground. This standardization makes precise calculation of a support for each cross-section useless.*
>
> *Further, the need to install the support immediately after excavation does not allow time to make calculations and fabricate the support. In order to arrive at a precise determination it would be necessary, in fact, to study each cross-section separately because it would differ from neighboring cross-sections with respect to the rock layers encountered, their dip and their deposition. It would be necessary to take a test specimen from each layer, determine its properties and the influence of these properties on neighboring layers. This would require a series of experiments and mathematical analyses whose solution, assuming that a solution is possible, would take up precious time during which the excavation would certainly have collapsed.*

Given these constraints, it is valuable to have a general albeit simplified appreciation of the nature of the interplay between the (variable) rock-mass and the installed support, and the effect of variation in assumed rock properties on the support loads.

The 'Convergence-Confinement' method is such a tool. Although the term was developed in the 1960's and 70s (see, for example, AFTES, French Association for Underground Works 1978), the method has been known at least since the paper by Fenner (1938). Application of the Convergence-Confinement method, as is discussed later in detail, requires a knowledge of the deformation characteristics of the ground and of the support.

Estimation of the mechanical response of a jointed rock-mass is one of the fundamental problems in rock mechanics. The Hoek-Brown criterion (Hoek and Brown 1980) for rock failure is widely used as an attempt to address the problem. The presence of joints and associated in situ geological effects (e.g., weathering and inhomogeneities) can considerably reduce the mechanical strength and stiffness of the rock-mass compared to the corresponding properties of intact specimens taken from the mass. The Hoek-Brown criterion 'adjusts' the strength properties of intact rock cores measured in triaxial tests in order to estimate the reduced strength that the rock-mass will exhibit in the field scale.

The following sections review the practical implementation of the Convergence-Confinement method to rock-masses that can be described by the Hoek-Brown failure criterion. Because of its importance in defining the strength and deformability properties of rock-masses, a detailed discussion of the Hoek-Brown failure criterion is presented as Appendix A to this paper.

Present addresses: Dr. Carlos Carranza-Torres, Consulting Engineer, Itasca Consulting Group Inc., 708 South Third St., Suite 310, Minneapolis, MN 55415, U.S.A. (cct@itascacg.com); Dr. Charles Fairhurst, Professor Emeritus, Department of Civil Engineering, University of Minnesota, Minneapolis, MN, U.S.A. (fairh001@tc.umn.edu)

www.elsevier.com/locate/tust

Tunnelling and Underground Space Technology, Vol. 15, No. 2, pp. 187–213, 2000
0886-7798/00/ $ - see front matter © 2000 Published by Elsevier Science Ltd.
All rights reserved.
PII: S0866-7798(00)00046-8

Pergamon

2. The Convergence-Confinement Method of Tunnel Design

As noted in the Introduction, the Convergence-Confinement method is a procedure that allows the load imposed on a support installed behind the face of a tunnel to be estimated. When a section of support is installed in the immediate vicinity of the tunnel face, it does not carry the full load to which it will be subjected eventually. A part of the load that is redistributed around the excavation is carried by the face itself. As the tunnel and face advance (i.e., away from the installed support), this 'face effect' decreases and the support must carry a greater proportion of the load that the face had carried earlier. When the face has moved well away from the support in question, it carries effectively, the full design load.

The problem is illustrated in Figure 1a. A cylindrical tunnel of radius R is driven (e.g., by the conventional drill-and-blast method) through a rock-mass that is assumed to be subject initially to a uniform (i.e., hydrostatic) stress field. A circular support is installed at a section *A—A'* located a distance L from the face of the tunnel (the support is assumed to be of unit length in the direction of the tunnel axis). The objective of the analysis is to determine the load that the rock-mass will transmit to the support at section *A—A'*, from the time of installation —indicated in Figure 1a— until the time when the face has moved ahead, sufficiently far that the 'face effect' has disappeared.

The variables involved in the analysis are shown in Figure 1b, which is a cross-section of the excavation at the position *A—A'* (the support has been 'removed' for clarity in this figure). The stress σ_o represents the hydrostatic far-field stress acting on the rock-mass. The radius R_{pl} indicates the extent of the 'failure' (or plastic) zone that develops around the tunnel (a discussion of the development of this failure region will be presented in Section 3).

To simplify the problem, it is assumed that all deformations occur in a plane perpendicular to the axis of the tunnel (i.e., the problem is two-dimensional plane strain) and that the radial displacement u_r and the pressure p_i—the latter representing the reaction of the support on the walls of the tunnel—are uniform at the section. Figure 1c shows a cross-section of a circular annular support of thickness t_c and external radius R installed at the section *A—A'*. The uniform pressure p_s represents the load transmitted by the rock-mass to the support; the radial displacement u_r represents the displacement induced by the load p_s. For compatibility of deformations at the rock support interface, the radial displacement of the support must equal the radial displacement of the rock wall u_r indicated in Figure 1b.

The basis of the Convergence-Confinement method is illustrated in the sequences (a) through (c) in Figure 2. The situation at the initial time t_0, when the lining is installed at section *A—A'*, is represented in the upper sketch (Figure 2a). At this instant, the section is located at a distance L from the face and the ground has converged radially by the amount u_r^0. It is assumed that, provided the face does not advance, the rock-mass transmits no load to the support — i.e., $p_s^0 = 0$ at this stage. (Time-dependent weakening, with associated deformation, is not considered in this analysis.)

As the tunnel advances to the right, the ground and the support (at section *A—A'*) deform together and the support receives part of the load that the face had been carrying previously. Figure 2b shows the situation at a time t when the section is located at the distance L_t from the face; at that moment, the ground has converged the amount $u_r^t > u_r^0$ and the rock-mass transmits the pressure p_s^t to the support.

Once the face of the tunnel has moved ahead far enough (Fig. 2c), the ground-support system at the section *A—A'* is in equilibrium and the support carries the final (or design) load p_s^D. At this time t_D, the effect of the face has disappeared and the support and ground have converged together by the final amount u_r^D.

As can be seen from Figure 2, determination of the load transferred to the support requires an analysis of the interaction of the load-deformation characteristics of the elements comprising the system, *(i)* the tunnel as it moves forward; *(ii)* the section of excavation perpendicular to the tunnel axis; and *(iii)* the support installed at that section.

The three basic components of the Convergence-Confinement method are, therefore, *(i)* the Longitudinal Deformation Profile (LDP); *(ii)* the Ground Reaction Curve (GRC); and *(iii)* the Support Characteristic Curve (SCC).

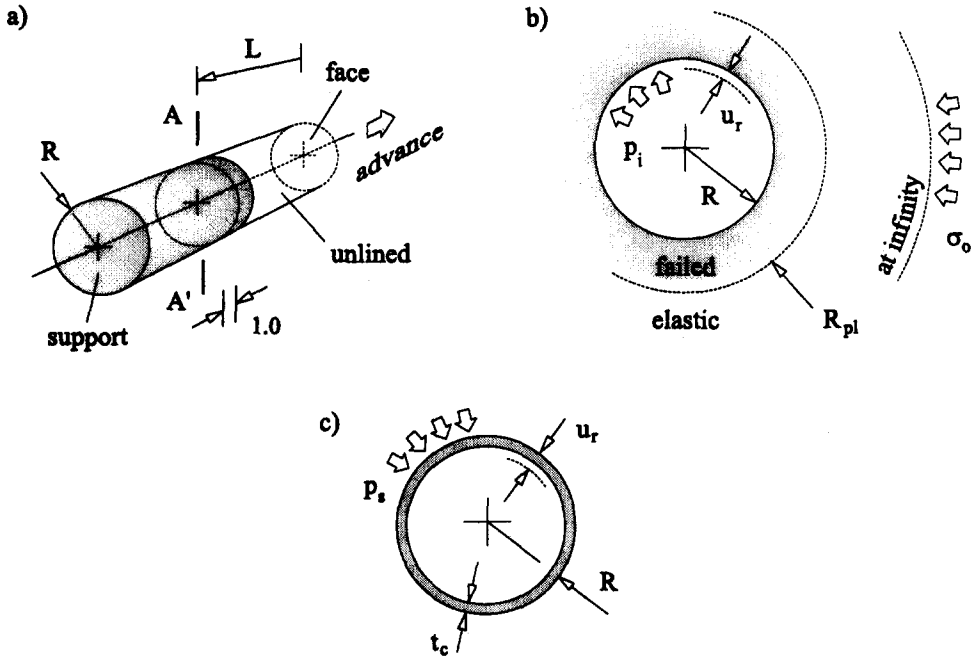

Figure 1. a) Cylindrical tunnel of radius R driven in the rock-mass. b) Cross-section of the rock-mass at section A—A'. c) Cross-section of the circular support installed at section A—A'.

The LDP is the graphical representation of the radial displacement that occurs along the axis of an *unsupported* cylindrical excavation —for sections located ahead of and behind the face. The upper diagram in Figure 3 represents such a profile. The horizontal axis indicates the distance x from the section analyzed to the tunnel face; the vertical axis indicates the corresponding radial displacement u_r (the right part of the diagram is included for use later in relating the LDP to the GRC and the SCC). The diagram indicates that at some distance *behind* the tunnel face the effect of the face is negligibly small, so that beyond this distance the unlined tunnel section has converged by the final amount u_r^M. Similarly, at some distance *ahead* of the face, the advancing tunnel has no influence on the rock-mass and the radial displacement is zero.

Considering now the section of unlined tunnel represented in Figure 1b, the GRC is defined as the relationship between the decreasing internal pressure p_i and the increasing radial displacement of the wall u_r. The relationship depends on the mechanical properties of the rock-mass and can be obtained from elasto-plastic solutions of rock deformation around an excavation (Section 3 discusses the construction of the GRC). The GRC is shown as the curve *OEM* in the lower diagram of Figure 3, extending from point O —where the internal pressure p_i is equal to the initial stress σ_o, to point M corresponding to the case where the internal pressure is equal to zero (i.e., the tunnel is unsupported) and the maximum closure (i.e., the radial displacement) u_r^M is the maximum possible. Point E defines the internal pressure p_i^{cr} and corresponding closure at which the elastic limit of the rock is reached (at the tunnel wall) —if the internal pressure falls below this value, a failed region of extent R_{pl} develops around the tunnel, as shown in Figure 1b.

The SCC is similarly defined as the relationship between the increasing pressure p_s on the support (shown in Fig. 1c) and the increasing radial displacement u_r of the support. This relationship depends on the geometrical and mechanical characteristics of the support (Section 4 discusses the construction of the SCC). The SCC is shown as the curve *KR* in the lower diagram of Figure 3. Point K corresponds to a support pressure equal to zero (i.e., when the support is first installed) and point R to the pressure p_s^{max} that produces failure of the support.

Interpretation of the interaction between the LDP, GRC and SCC allows us to define the pressure p_s that the ground transmits to the support as the face advances. To illustrate the procedure, consider again the sequences *a)* through *c)* illustrated in Figure 2. Installation of the support at section *A—A'* at time t_0 in Figure 2a, corresponds in the LDP of Figure 3 as point I of coordinates $x = L$ and $u_r = u_r^0$. Point J on the right side of the diagram has a horizontal coordinate $u_r = u_r^0$ and defines point K of the SCC in the diagram below. As long as the face does not move, stability is maintained solely by the ability of the face to carry the load redistributed by excavation. Thus, the vertical segment *KN* in the lower diagram of Figure 3 corresponds to the pressure taken by the face at time t_0. (Again, note that time dependent weakening of the rock-mass is not considered here.)

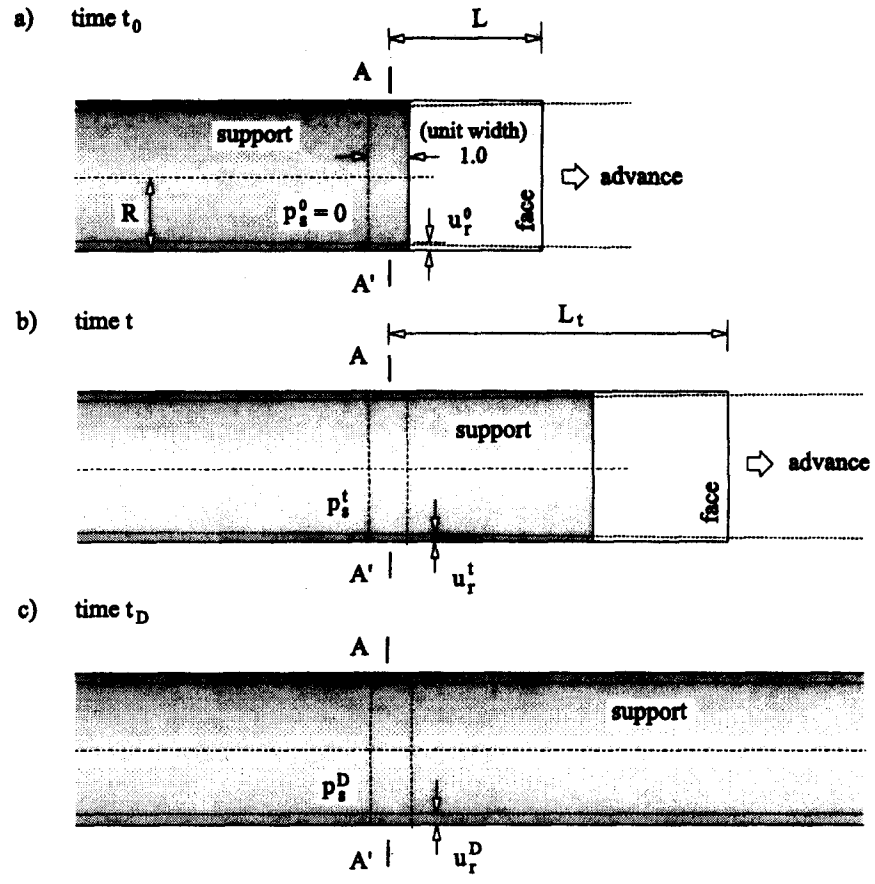

Figure 2. Loading of the support at section A—A' due to progressive advance of the tunnel face.

As the face advances in Figure 2, both the support and excavation deform by the same amount —with the pressure p_s on the support increasing and the confining effect p_i on the periphery of the tunnel decreasing.

At time t_D in Figure 2c, when the supporting effect of the face has disappeared completely, the system reaches equilibrium at point D in the lower diagram of Figure 3—i.e. at the intersection of the GRC and the SCC. The pressure p_s^D defined by point D then represents the final pressure (or design load) that the rock transmits to the support.

Inspection of the LDP, GRC and SCC in Figure 3 leads to two conclusions of practical interest:

i) the support will not be subject to a radial pressure larger than p_s^L —defined by point L in the lower diagram. This pressure would be achieved only in the hypothetical case of an infinitely rigid support installed at the face itself —i.e., the SCC would be a vertical one, starting from point H; and

ii) a support will take no load if placed beyond point M, since the maximum possible convergence has occurred already.

These two cases correspond to the two limiting cases of load that the rock-mass can transmit to the support. In general, as is seen from the LDP, GRC and SCC in Figure 3, the further that the support is installed from the tunnel face, the lower the final load p_s^D on the support (assuming, again, that no time-dependent weakening or disintegration of the rock-mass occurs).

3. Construction of the Ground Reaction Curve

The Ground Reaction Curve (GRC) shown in Figure 3 can be constructed from the elasto-plastic solution of a

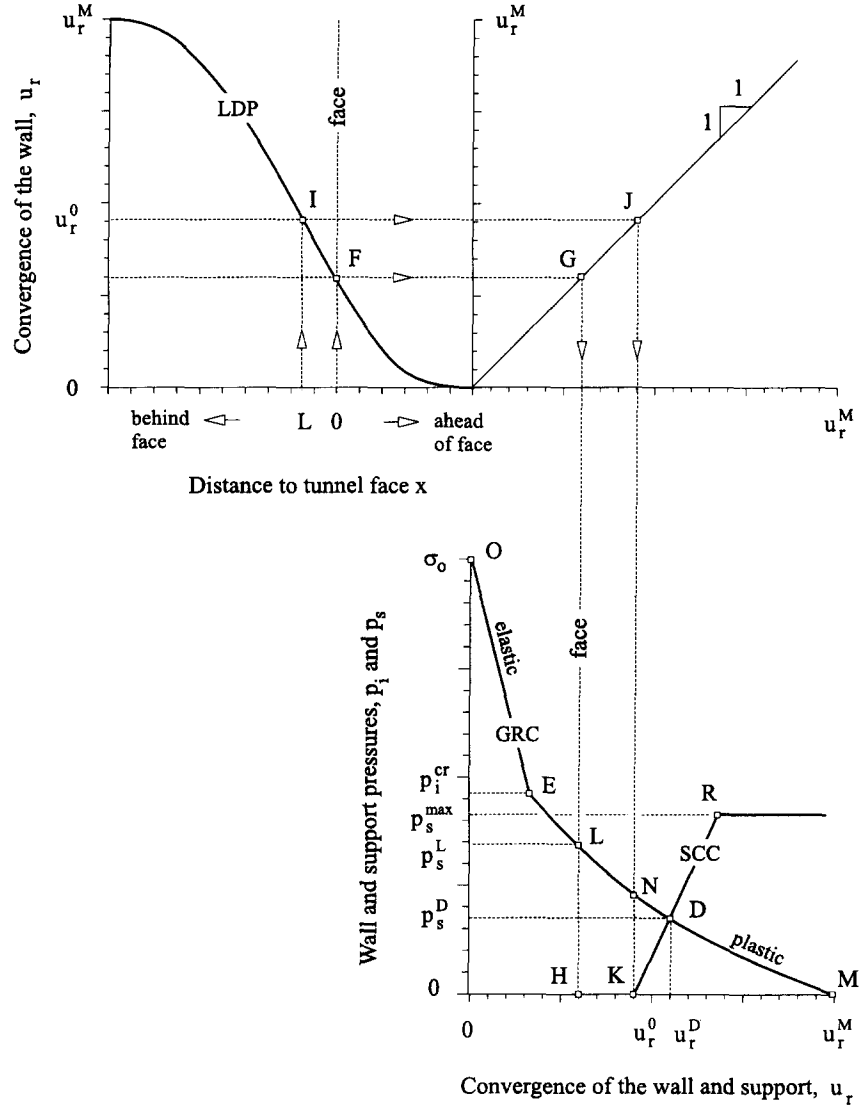

Figure 3. Schematic representation of the Longitudinal Deformation Profile (LDP), Ground Reaction Curve (GRC) and Support Characteristic Curve (SCC).

circular opening subject to uniform (i.e., hydrostatic) far-field stresses and uniform internal pressure (see Fig. 1b). Several solutions of this type, based on the Hoek-Brown failure criterion for the rock, have been published in the past. Some of these solutions include approximations in the equations of deformations to simplify the problem —see for example Brown (1983); others resort directly to numerical treatment to obtain a relationship between internal pressure and radial deformation (for example, Wang 1996).

In the present work, an analytical solution derived by Carranza-Torres and Fairhurst (1999) will be considered. The solution is based on the 'general' form of the Hoek-Brown criterion proposed by Londe (1988) —the reader is referred to Appendix A for a detailed review of the Hoek-Brown failure criterion and the coefficients characterizing the strength and deformability of the rock-mass, that will be used in the equations presented this section.

Consider the section of a cylindrical tunnel of radius R subject to uniform far-field stress σ_o and internal pressure p_i shown in Figure 1b. The rock-mass is assumed to satisfy the Hoek-Brown failure criterion defined by equation (A-2); the variables characterizing the strength of the rock-mass are the unconfined compressive strength σ_{ci}, the intact rock parameter m_i, and the rock-mass parameters m_b and s discussed in Appendix A (as mentioned there, the analysis assumes the parameter a to be 0.5).

The uniform internal pressure p_i and far-field stress σ_o can be 'scaled' according to the transformation (A-8), to give the scaled internal pressure P_i and far-field stress S_o, respectively,

$$P_i = \frac{p_i}{m_b \sigma_{ci}} + \frac{s}{m_b^2} \quad (1)$$

$$S_o = \frac{\sigma_o}{m_b \sigma_{ci}} + \frac{s}{m_b^2} \quad (2)$$

The pressure p_i^{cr}, defined by point E in the GRC of Figure 3, marks the transition from elastic to plastic behavior of the rock-mass —i.e., for an internal pressure $p_i \geq p_i^{cr}$, the rock remains elastic, and for $p_i < p_i^{cr}$, a plastic region of radius R_{pl} develops around the tunnel (see Fig, 1b).

The scaled critical (internal) pressure P_i^{cr} for which the elastic limit is achieved is given by the following expression:

$$P_i^{cr} = \frac{1}{16}\left[1-\sqrt{1+16S_o}\right]^2 \tag{3}$$

The actual (i.e., non-scaled) critical pressure is found from the inverse of equation (1),

$$p_i^{cr} = \left[P_i^{cr} - \frac{s}{m_b^2}\right] m_b\, \sigma_{ci} \tag{4}$$

Provided $p_i \geq p_i^{cr}$, the relationship between the radial displacements u_r^{el} and internal pressure p_i in the elastic part of the GRC (i.e., segment *OE* in Fig. 3) is given by the equation,

$$u_r^{el} = \frac{\sigma_o - p_i}{2G_{rm}} R \tag{5}$$

where G_{rm} is the shear modulus of the rock-mass defined by equation (A-10).

For values of internal pressure $p_i < p_i^{cr}$, the extent of the plastic region R_{pl} that develops around the tunnel is

$$R_{pl} = R\, \exp\left[2\left(\sqrt{P_i^{cr}} - \sqrt{P_i}\right)\right] \tag{6}$$

To define the plastic part of the Ground Reaction Curve (i.e., the curve *EM* in the GRC of Figure 3), a flow rule for the material is needed. The flow rule defines the relationship between the strains that produce distortion and those that produce volumetric changes, as plastic deformation occurs in the material—see, for example, Atkinson (1993). In underground excavation practice, the flow rule is usually assumed to be linear, with the magnitude of volumetric change characterized by a 'dilation' angle ψ, such that, if $\psi = 0°$, the material undergoes no change in volume during plastic deformation; if $\psi > 0°$, the volume increases during plastic deformation.

In the solution described here, the flow rule will be characterized by a dilation coefficient K_ψ, that is computed from the dilation angle, ψ, according to the expression $K_\psi = [1 + \sin\psi]/[1 - \sin\psi]$. Note, for example, that for $\psi = 0°$, the dilation coefficient is $K_\psi = 1$ and for $\psi = 30°$, the coefficient is $K_\psi = 3$.

With the flow rule characterized by the dilation coefficient K_ψ, the plastic part of the GRC —i.e., the segment *EM* in Figure 3—is given by

$$\frac{u_r^{pl}}{R}\frac{2G_{rm}}{\sigma_o - p_i^{cr}} = \frac{K_\psi - 1}{K_\psi + 1} + \frac{2}{K_\psi + 1}\left(\frac{R_{pl}}{R}\right)^{K_\psi + 1} + \frac{1-2\upsilon}{4(S_o - P_i^{cr})}\left[\ln\left(\frac{R_{pl}}{R}\right)\right]^2 - \left[\frac{1-2\upsilon}{K_\psi + 1}\frac{\sqrt{P_i^{cr}}}{S_o - P_i^{cr}} + \frac{1-\upsilon}{2}\frac{K_\psi - 1}{(K_\psi + 1)^2}\frac{1}{S_o - P_i^{cr}}\right] \times \left[(K_\psi + 1)\ln\left(\frac{R_{pl}}{R}\right) - \left(\frac{R_{pl}}{R}\right)^{K_\psi + 1} + 1\right] \tag{7}$$

where ν is Poisson's ratio for the rock-mass.

Hoek and Brown (1997) suggest that in some cases the assumption of no plastic volume-change for the rock-mass may be more appropriate. For the case of non-dilating rock-masses, characterized by the coefficient $K_\psi = 1$, equation (7) becomes

$$\frac{u_r^{pl}}{R}\frac{2G_{rm}}{\sigma_o - p_i^{cr}} = \left[\frac{1-2\upsilon}{2}\frac{\sqrt{P_i^{cr}}}{S_o - P_i^{cr}} + 1\right]\left(\frac{R_{pl}}{R}\right)^2 + \frac{1-2\upsilon}{4(S_o - P_i^{cr})}\left[\ln\left(\frac{R_{pl}}{R}\right)\right]^2 - \frac{1-2\upsilon}{2}\frac{\sqrt{P_i^{cr}}}{S_o - P_i^{cr}}\left[2\ln\left(\frac{R_{pl}}{R}\right) + 1\right] \tag{8}$$

To illustrate the construction of Ground Reaction Curves using equations (1) through (8), let us consider the case shown in Figure 4 of an *unsupported* section *A—A'* of a tunnel, radius *R*, located at a distance of 10 *R* behind the face of the tunnel (as will be discussed in Section 5), a distance of 10 *R* is large enough that the face has no further effect on the section).

We wish to determine the radial convergence and the extent of the plastic region as the internal pressure p_i is reduced from the (initial) in-situ stress value σ_o towards zero.

In this particular example, the radius of the tunnel is $R = 1$ m, the initial stress field is $\sigma_o = 7.5$ MPa and the properties of the intact rock are $\sigma_{ci} = 20$ MPa and $m_i = 15$. Rock-masses of decreasing quality, characterized by GSI values equal to 50, 40 and 30, are considered. The parameters defining the strength and deformability of the rock-mass according to the Hoek-Brown criterion are computed from equations (A-3) through (A-5) and (A-9) through (A-10) are listed in Figure 4a.

The ground reaction curves constructed using expressions (1) through (8) for *GSI* values equal to 50, 40 and 30 are shown in Figure 4b. The dashed-line curves represent the corresponding extent R_{pl} of the failure zone (the values of R_{pl} are read on the vertical axis on the right side of the diagram). Points *A*, *B* and *C* represent the condition at which the elastic limit of the rock-mass is reached. Note that these points are associated with a failure region of extent $R_{pl} = R = 1$ m (i.e., a failure zone that is about to start to develop around the tunnel).

To validate the analytical results presented in Figure 4, a numerical analysis was carried out with the finite difference code FLAC^{3D} (Itasca Consulting Group 1997). The models were set up and solved for values of internal pressures p_i =0.5, 1.0 and 1.5 MPa. The values of radial displacement obtained from these models, represented as open squares in Figure 4b, are in good agreement with the analytical results.

4. Construction of Support Characteristic Curves

The Support Characteristic Curve (SCC) shown in Figure 3 can be constructed from the elastic relationship between the applied stress p_s and the resulting closure u_r for a section of the support of unit length in the direction of the tunnel (see Fig. 1c).

If the elastic stiffness of the support is denoted by K_s, the elastic part of the SCC —i.e., segment *KR* in Figure 3, can be computed from the expression,

$$p_s = K_s\, u_r \tag{9}$$

Note that from equation (9), the unit of the stiffness K_s is pressure divided by length (e.g., MPa/m if the stresses are expressed in MPa and the displacements in meters).

The plastic part of the SCC in Figure 3—i.e., the horizontal segment starting at point *R*, is defined by the maximum pressure p_s^{max} that the support can accept before collapse.

The following subsections present the equations needed to compute the maximum pressure p_s^{max} and the elastic stiffness K_s for three different support systems:

i) shotcrete or concrete rings,

ii) blocked steel sets and

iii) ungrouted bolts and cables.

These equations have been adapted from Hoek and Brown (1980) and Brady and Brown (1985). The reader is referred to the original source for a detailed description of each of these support systems.

4.1 Shotcrete or Concrete Rings

Considering the closed ring of shotcrete or concrete represented in Figure 5a, the maximum pressure provided by the support is

a)

R = 1 m
σ_o = 7.5 MPa
σ_{ci} = 20 MPa
m_i = 15
ν = 0.25
ψ = 30°

GSI	m_b	s	G_{rm} (GPa)
50	2.5	3.9×10^{-3}	1.8
40	1.8	1.3×10^{-3}	1.0
30	1.2	0.4×10^{-3}	0.6

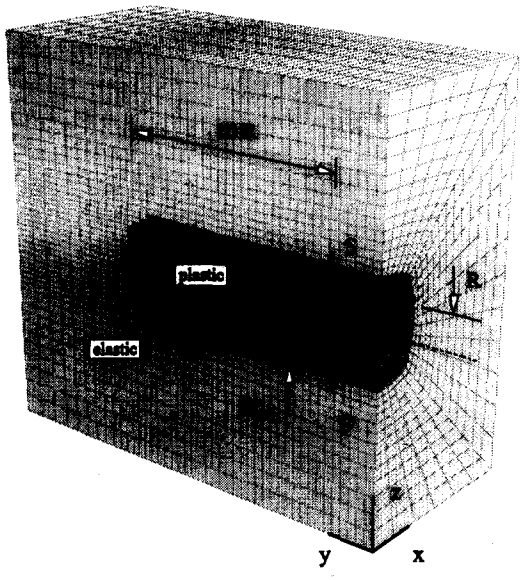

b)

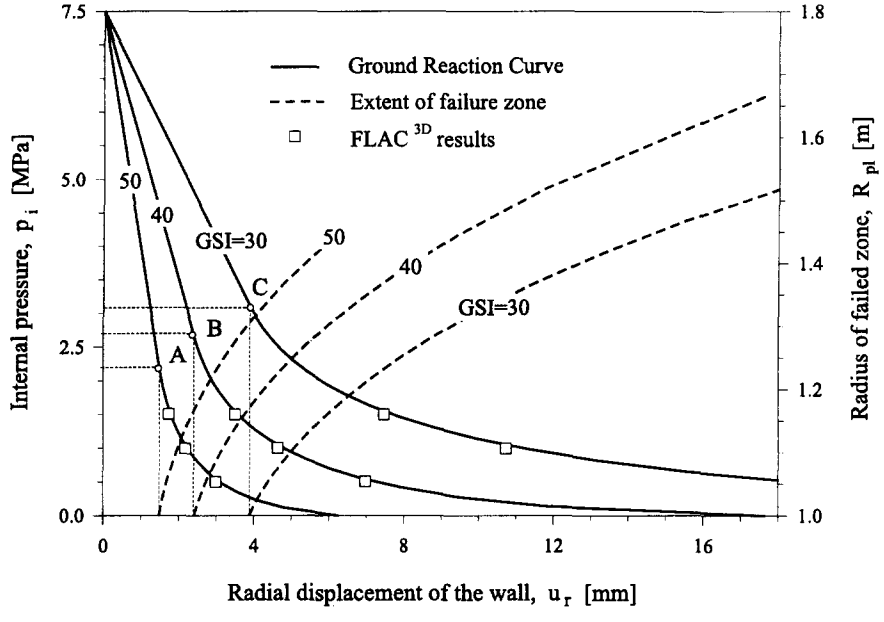

Figure 4. a) Analysis of the convergence and the extent of the plastic zone for a section of tunnel located well behind the tunnel face. b) Ground Reaction Curves and extent of failure curves for section A-A' in the model—for GSI values of 50, 40 and 30. The points A, B and C represent the elastic limit in each GRC. The open squares in the diagram correspond to results obtained with FLAC 3D.

Table 1. Values of σ_{cc} and E_c for dry and wet shotcrete mixtures after 1 and 28 days (after Singh and Bortz 1975).

Type of mixture	σ_{cc} [MPa]	E_c [MPa]
Dry (1 day)	20.3	$13.6 \times 10^3 - 23.4 \times 10^3$
(28 days)	29.6	$17.8 \times 10^3 - 23.1 \times 10^3$
Wet (1 day)	18.9 – 20.3	$12.3 \times 10^3 - 28.0 \times 10^3$
(28 days)	33.3 – 39.4	$23.8 \times 10^3 - 35.9 \times 10^3$

Cement type III. Maximum aggregate size 13 mm. Mix design –expressed as a percentage of total bulk weight: *i)* Dry mixture: 17.9% cement; 29.9% coarse aggregate; 52.2% sand. *ii)* Wet mixture: 16.7% cement; 27.9% coarse aggregate; 48.7% sand; 6.7% water.

Table 2. Values of σ_{cc} and E_c for concrete mixtures used in the construction industry (after Leonhardt 1973).

Designation	σ_{cc} [MPa]	E_c [MPa]
Bn 150	14.7	25.5×10^3
Bn 250	24.5	29.4×10^3
Bn 350	34.3	33.3×10^3
Bn 450	44.1	36.3×10^3
Bn 550	53.9	38.2×10^3

Properties after 28 days, obtained from tests on cubic samples of 200 mm side. The strength of concrete at the early age of 7 days is approximately 80% of the σ_{cc} values listed above.

Table 3. Values of Young's modulus E_s and yield strength σ_{ys} for different steel types (adapted from Gieck 1977).

Designation	E_s [MPa]	σ_{ys} [MPa]
St 37–11	210×10^3	80 – 120
St 50–11	210×10^3	100 – 150
GS 38	220×10^3	80 – 100

The ranges of admissible stress σ_{ys} listed above are for static-compressive loads. This assumes a safety coefficient of 1.75 with respect to the yield strength.

$$p_s^{max} = \frac{\sigma_{cc}}{2}\left[1 - \frac{(R - t_c)^2}{R^2}\right] \tag{10}$$

The elastic stiffness is

$$K_s = \frac{E_c}{(1-\nu_c)R} \frac{R^2 - (R - t_c)^2}{(1-2\nu_c)R^2 + (R - t_c)^2} \tag{11}$$

where

- σ_{cc} is the unconfined compressive strength of the shotcrete or concrete [MPa];
- E_c is Young's Modulus for the shotcrete or concrete [MPa];
- ν_c is Poisson's ratio for the shotcrete or concrete [dimensionless];
- t_c is the thickness of the ring [m];
- R is the external radius of the support [m] (taken to be the same as the radius of the tunnel)

Typical values for σ_{cc} and E_c for *dry* and *wet* shotcrete mixtures[1)] are given in Table 1. Poisson's ratio for the shotcrete is usually assumed to be $\nu_c = 0.25$. The thickness t_c of the shotcrete depends on the roughness of the surface after blasting and scaling. When the shotcrete is applied as a temporary support system, the thickness usually varies between 50 and 100 mm.

For pre-cast or cast-in-place concrete support, the parameters σ_{cc} and E_c depend mainly on the type of cement and aggregate used in the mixture. Table 2, adapted from Leonhardt (1973), lists values of σ_{cc} and E_c for typical concrete mixtures used in the construction industry. Poisson's ratio ν_c for concrete varies between 0.15 and 0.25; the value $\nu_c = 0.2$ is normally used in practice (Leonhardt 1973). The thickness t_c for pre-cast or cast-in-place support is usually larger than that for shotcrete, partly because structural steel reinforcement is commonly used (structural steel reinforcement requires a sufficient cover of concrete to protect the steel from corrosion).

4.2 Blocked Steel Set

Considering steel sets spaced a unit length apart in the direction of the tunnel axis and tightened against the rock by wood blocks that are equally spaced circumferentially—as shown in Figure 5b— the maximum pressure that the system can sustain is

$$p_s^{max} = \frac{3}{2}\frac{\sigma_{ys}}{S R \theta}\frac{A_s I_s}{3I_s + D A_s [R - (t_B + 0.5D)](1 - \cos\theta)} \tag{12}$$

The elastic stiffness is

$$\frac{1}{K_s} = \frac{S R^2}{E_s A_s} + \frac{S R^4}{E_s I_s}\left[\frac{\theta(\theta + \sin\theta\cos\theta)}{2\sin^2\theta} - 1\right] + \frac{2S\theta t_B R}{E_B B^2} \tag{13}$$

where

- B is the flange width of the steel set and the side length of the square block [m]
- D is the depth of the steel section [m]
- A_s is the cross-sectional area of the section [m²]
- I_s is the moment of inertia of the section [m⁴]
- E_s is Young's modulus for the steel [MPa]
- σ_{ys} is the yield strength of the steel [MPa]
- S is the steel set spacing along the tunnel axis [m]
- q is half the angle between blocking points [radians]
- t_B is the thickness of the block [m]
- E_B is Young's modulus for the block material [MPa]
- R is the tunnel radius [m]

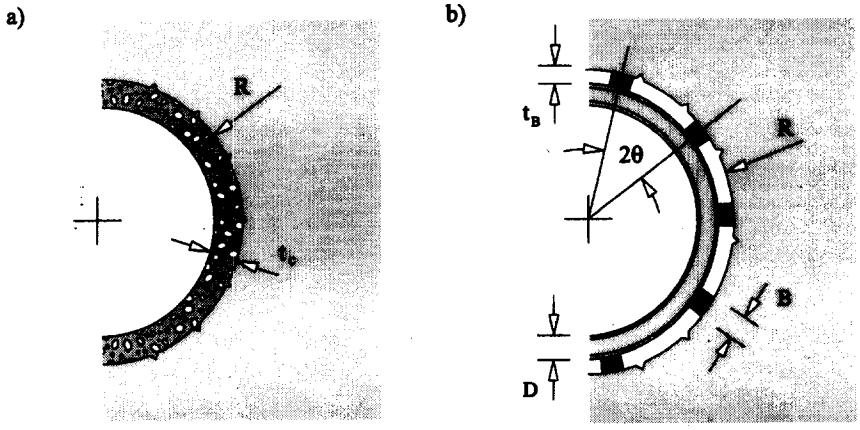

Figure 5. Schematic representation of sections of a) shotcrete or concrete rings and b) blocked steel sets (adapted from Brady and Brown 1983).

1) The distinction between *dry* and *wet* mixtures comes from the moment at which water is added to the cement/sand mixture. In the former, sand and cement are mixed dry and water is added at the nozzle of the shotcrete equipment. In the latter, sand, cement and water are mixed at the same time and the mixture pumped to the nozzle for application.

Table 4. Values of D, B, A_s and I_s for typical steel sections (adapted from CONSTRADO 1988).

Universal Beams

Section	D [mm]	B [mm]	A_s [m^2]	I_s [m^4]	t [mm]	T [mm]
457 × 152	461	153	9.50×10^{-3}	324.35×10^{-6}	9.9	17.0
406 × 140	402	142	5.90×10^{-3}	156.47×10^{-6}	6.9	11.2
356 × 127	353	126	4.94×10^{-3}	100.87×10^{-6}	6.5	10.7
305 × 127	304	124	4.75×10^{-3}	71.62×10^{-6}	7.2	10.7
254 × 102	260	102	3.62×10^{-3}	40.08×10^{-6}	6.4	10.0
203 × 133	203	133	3.23×10^{-3}	23.56×10^{-6}	5.8	7.8

Joists

Section	D [mm]	B [mm]	A_s [m^2]	I_s [m^4]	t [mm]	T [mm]
203 × 102	203	102	3.23×10^{-3}	22.94×10^{-6}	5.8	10.4
152 × 89	152	89	2.18×10^{-3}	8.81×10^{-6}	4.9	8.3
127 × 76	127	76	1.70×10^{-3}	4.76×10^{-6}	4.5	7.6
102 × 64	102	64	1.23×10^{-3}	2.18×10^{-6}	4.1	6.6
89 × 89	89	89	2.94×10^{-3}	3.07×10^{-6}	9.5	9.9
76 × 76	76	76	1.63×10^{-3}	1.59×10^{-6}	5.1	8.4

Universal beams, in contrast to *joists*, have flanges of the same thickness throughout. The figure on the right shows a typical joist section with non-parallel flanges (the thickness T is measured at the mid-distance on the flange). Note that the values of moment of inertia I_s listed above are with respect to the axis x–x indicated in the figure. This considers that the shortest side (the flange of width B) is in contact with the wood block placed between the rock surface and the steel section (see Figure 5b).

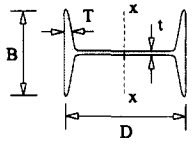

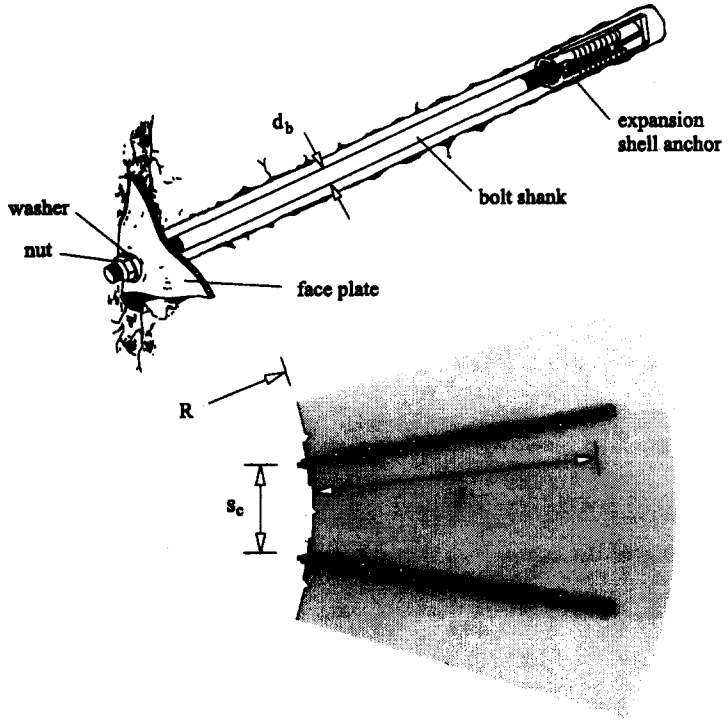

Figure 6. Representation of an ungrouted mechanical-anchored bolt (adapted from Stillborg 1994 and Hoek and Brown 1980).

For the case of blocked steel sets spaced at intervals d_s other than unity, both the maximum stress p_s^{max} given by equation (12) and the stiffness K_s given by equation (13) should be divided by (d_s/1.0 m).

Values of Young's modulus E_s and yield strength σ_{ys} for different types of steel are listed in Table 3.

Values of D, B, A_s and I_s for typical sections of steel are given in Table 4.

The angle θ in equations (12) and (13) can be computed as $\theta = \pi/n_B$, where n_B is the total number of equally spaced blocks installed in the cross-section.

Young's Modulus for the wood block depends on the type of wood used and on the tightness of the block at installation. For hard woods (e.g., ash, maple, oak) Young's Modulus is typically $E_b = 10 \times 10^3$ MPa and for conifers (e.g., pine, cypress, cedar) it is $E_b = 7 \times 10^3$ MPa (Derucher and Korfiatis 1988). In order to take into account the tightness of the block at installation, Hoek and Brown (1980) suggest the values $E_b = 10 \times 10^3$ MPa for stiff blocking and $E_b = 500$ MPa for soft blocking.

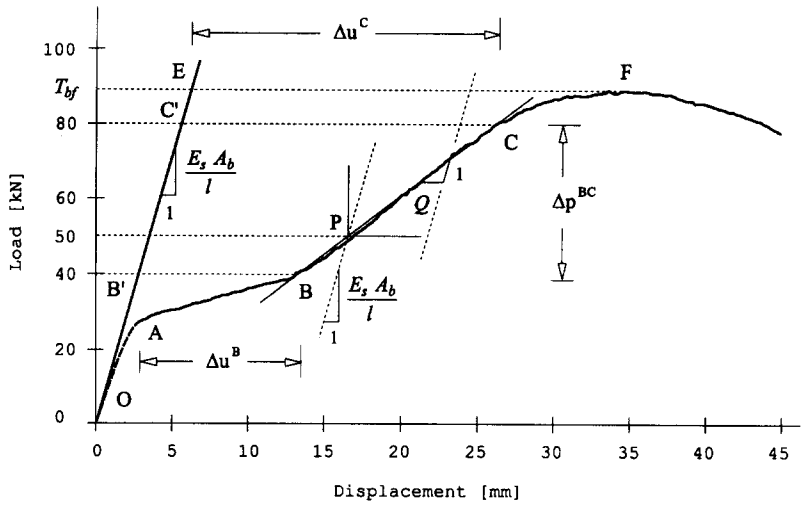

Figure 7. Results of a pull-out test performed on a mechanically anchored bolt (adapted from Stillborg 1994).

4.3 Ungrouted Bolts and Cables

The sketches in Figure 6 represent mechanically anchored bolts installed in the rock-mass surrounding a circular tunnel of radius R. Assuming that the bolts are equally spaced in the circumferential direction, the maximum support pressure provided by this support system is

$$p_s^{max} = \frac{T_{bf}}{s_c\, s_l} \tag{14}$$

The stiffness is

$$\frac{1}{K_s} = s_c\, s_l \left[\frac{4l}{\pi d_b^2 E_s} + Q\right] \tag{15}$$

where

- d_b is the bolt or cable diameter [m];
- l is the free length of the bolt or cable [m];
- T_{bf} is the ultimate load obtained from a pull-out test [MN];
- Q is a deformation-load constant for the anchor and head [m/MN];
- E_s is Young's Modulus for the bolt or cable [MPa];
- s_c is the circumferential bolt spacing [m];
- s_l is the longitudinal bolt spacing [m].

Equation (15) assumes that the reaction forces developed by the bolt are concentrated at the ends of the bar; therefore the equation should not be applied in the case of grouted bolts —for which the load transfer is distributed throughout the length of the shank.

The circumferential bolt spacing s_c in equations (14) and (15) can be computed as $s_c = 2\pi R / n_b$, where n_b is the total number of equally spaced bolts or cables installed in the cross-section.

Typical values of Young's modulus for the steel are listed in Table 3.

To illustrate how the constants T_{bf} and Q are obtained from testing of bolts, consider the diagram in Figure 7. This shows the results of a pull-out test performed by Stillborg (1994) on a mechanically anchored bolt 16 mm in diameter and 3 m long installed in a concrete block of compressive strength $\sigma_{cc} = 60$ MPa (details of the test can be found in the original article). The load applied to the bolt is shown on the vertical axis and the bolt deformation on the horizontal axis. The line *OE* corresponds to the elastic deformation of the shank (see Fig. 6). The curve *OABCF* shows the total deformation measured at the wall of the concrete block — this includes the deformation of the shank, anchor, plate, washer and nut.

The high rate of displacement over the portion *AB* of the curve is associated with the initial compliance of the plate, washer and nut assembly. The steeper portion *BC* is associated with deformation of the bolt shank and the anchor. At point *C* in the curve, the bolt starts to yield and at point *F* the bolt fails. The constant T_{bf} in equation (14) is therefore defined by point *F* in Figure 7.

In practice, the bolt will usually be pre-tensioned during installation, in order to avoid the initial 'flat' segment *AB* associated to compliance of the plate and its associated components. The level of pre-tension should be sufficient to fully 'seat' the plate, washer and nut. For the results presented in Figure 7, for example, an appropriate level of pre-tensioning would be between 40 and 60 kN. Thus if a pre-tension of 50 kN is applied, the effect is to move the origin of the (subsequent) load-deformation curve from point *O* to point *P*.

The constant Q in equation (15) is the rate of deformation for the portion *BC* in Figure 7—this disregards the elastic deformation of the shank that is already accounted by the first term within brackets in equation (15).

Table 5. Values of the ultimate load T_{bf} and the deformation-load constant Q for bolts of different diameters d_b and lengths l (adapted from Hoek and Brown 1980).

d_b [mm]	l [m]	T_{bf} [MN]	Q [m/MN]
16	1.83	0.058	0.241
19	1.83	0.089	0.024
22	3.00	0.196	0.042
25	1.83	0.254	0.143

Values determined for *expansion shell* bolts in field tests. The rock types are: *i)* shale for the 16 mm bolt; *ii)* sandstone for the 22 mm bolt; *iii)* granite for the 25 mm bolt.

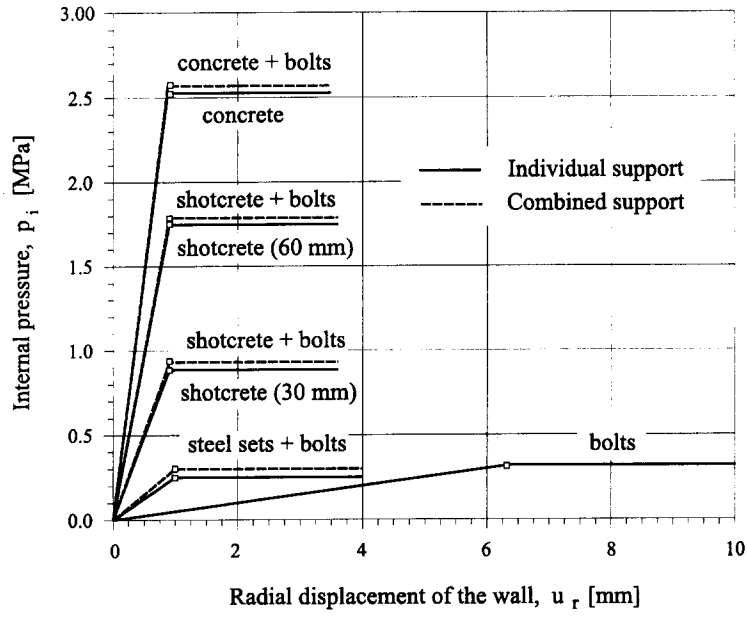

Individual support systems

Support type	p_s [MPa]	K_s [MPa/m]	u_r^{max} [m]
Shotcrete (t_c = 30 mm)	0.89	0.984×10^3	0.90×10^{-3}
Shotcrete (t_c = 60 mm)	1.75	2.019×10^3	0.87×10^{-3}
Concrete (t_c = 75 mm)	2.53	2.893×10^3	0.87×10^{-3}
Steel sets (127 × 76)	0.25	0.261×10^3	0.95×10^{-3}
Bolts (19 mm diameter)	0.32	0.050×10^3	6.36×10^{-3}

Combined support systems

Support type	p_s [MPa]	K_s [MPa/m]	u_r^{max} [m]
Shotcrete (30 mm) + Bolts	0.93	1.034×10^3	0.90×10^{-3}
Shotcrete (60 mm) + Bolts	1.79	2.069×10^3	0.87×10^{-3}
Concrete + Bolts	2.57	2.943×10^3	0.87×10^{-3}
Steel sets + Bolts	0.30	0.311×10^3	0.95×10^{-3}

Mechanical and geometrical properties considered for the supports: *i)* Shotcrete, σ_{cc} = 30 MPa, $E_c = 30 \times 10^3$ MPa, $\nu = 0.25$, t_c = 30 mm and t_c = 60 mm. *ii)* Concrete, σ_{cc} = 35 MPa, $E_c = 35 \times 10^3$ MPa, $\nu = 0.2$, t_c = 75 mm. *iii)* Blocked steel sets, B = 76 mm, D = 127 mm, $A_s = 1.70 \times 10^{-3}$ m^2, $I_s = 4.76 \times 10^{-6}$ m^4, $E_s = 210 \times 10^3$ MPa, σ_{ys} = 150 MPa, S = 1 m, $\theta = \pi/10$ rad (10 blocks), t_B = 75 mm, $E_b = 10 \times 10^3$ MPa. *iii)* Ungrouted bolts, d_b = 19 mm, l = 2 m, T_{bf} = 0.1 MN, Q = 0.03 m/MN, $E_s = 210 \times 10^3$ MPa, s_c = 0.63 m (10 bolts), s_l = 0.50 m.

Figure 8. Support Characteristic Curves for various support systems applied to a tunnel of radius R = 1 m.

Considering the magnitudes Δp^{BC}, Δu^B and Δu^C indicated in the diagram, the constant Q can be computed as

$$Q = \frac{\Delta u^C - \Delta u^B}{\Delta p^{BC}} \tag{16}$$

Ideally the values of T_{bf} and Q should be obtained from pull-out tests performed directly on bolts installed on the rock in situ. The values obtained in this way will depend on the type of rock and the mechanical characteristics of the bolt being tested. Hoek and Brown (1980) list reference values for T_{bf} and Q obtained from tests in different rock types. Some of these values are presented in Table 5 (these are for bolts of diameter 16, 19, 22 and 25 mm and lengths of 1.83 and 3.0 m).

4.4 Combined Effect of Support Systems

If more than one of the support systems described earlier is installed at the same location, their combined effect can be determined by adding the stiffnesses (i.e., the slope of the load vs. deformation curve) for each of the individual supports. This has the effect of increasing the slope of the elastic part of the SCC—the segment *KR* in Figure 3.

Consider, for example, the case in which two supports —characterized by maximum pressures p_{s1}^{max} and p_{s2}^{max} and elastic stiffnesses K_{s1} and K_{s2}, respectively, are installed in a section of tunnel. The stiffness K_s for the two systems acting together can be computed as $K_s = K_{s1} + K_{s2}$. This value is assumed to remain valid until one of the two supports achieves its maximum possible elastic deformation u_r^{max}—computed as $u_{r1}^{max} = p_{s1}^{max}/K_{s1}$ and $u_{r2}^{max} = p_{s2}^{max}/K_{s2}$, respectively (see equation 9). The combined support system is assumed to fail at that point. The support with the lowest value of u_r^{max} determines the maximum support pressure available for the two supports acting together.

Figure 8 shows the SCC for four types of support: shotcrete (with two different thicknesses), concrete, steel sets and ungrouted bolts for a tunnel of radius R = 1 m. The figure also considers the combined effect of two supports acting together: concrete and bolts; shotcrete and bolts; and steel sets and bolts. These SCC's were evaluated using the equations presented in Sections 4.1 through 4.3 (the values considered for the variables are listed in the lower part of the figure.)

For this particular problem, as seen in Figure 8, the SCC for steel sets is considerably below that for shotcrete and concrete linings. This is due to the dominant role played by the (compliant) wood blocking in the system. The lowest values of stiffness K_s —and therefore the maximum deformation u_r^{max}, corresponds to the bolts.

For the combined support systems, the failure is controlled by the stiffer shotcrete, concrete or steel set support types (compare the values of u_r^{max} listed in both tables). There is a slight improvement in the support capacity p_s^{max} and the stiffness K_s when two supports are considered acting together.

5. Construction of the Longitudinal Deformation Profile

The Longitudinal Deformation Profile (LDP) discussed in Section 2 is an important component of the Convergence-Confinement method. It provides insight into how quickly the support begins to interact with the rock-mass behind the face of the tunnel (i.e., it defines the point K in Fig. 3).

When the far-field stresses acting on the rock-mass are assumed to be uniform, the profile of radial displacements along the axis of the tunnel can be computed from numerical models of the problem shown in Figure 9a. The figure

represents a longitudinal cross-section of an unlined tunnel of radius R in the vicinity of the face. At a distance x from the face the radial displacement is u_r. When the distance x is large enough, the radial displacement reaches the maximum value u_r^M. For negative values of x (i.e., ahead of the face), the radial displacement decreases and the displacement becomes essentially zero at some finite distance ahead of the face.

From elastic models of the problem represented in Figure 9a, Panet (1995) suggests the following relationship between radial displacements and distance to the face:

$$\frac{u_r}{u_r^M} = 0.25 + 0.75\left[1 - \left(\frac{0.75}{0.75 + x/R}\right)^2\right] \qquad (17)$$

This relationship (17), that applies to positive values of x, is plotted in Figure 9b. The horizontal axis of the diagram represents the ratio x/R and the vertical axis represents the ratio u_r/u_r^M.

Chern et al. (1998) present measured values of convergence in the vicinity of the face for a tunnel in the Mingtam Power Cavern project. The measured data are plotted as dots in Figure 9b. Based on this data, Hoek (1999) suggests the following empirical best-fit relationship between radial displacement of the tunnel and distance to the face:

$$\frac{u_r}{u_r^M} = \left[1 + \exp\left(\frac{-x/R}{1.10}\right)^{-1.7}\right] \qquad (18)$$

The relationship (18) is also plotted in Figure 9b. Analysis of the curves defined by equations (17) and (18) indicates that the maximum radial displacement occurs at approximately 8 tunnel radii behind the face of the tunnel, and that the radial deformation is zero at approximately 4 tunnel radii ahead the face. At the face itself, the radial displacement is approximately 30% of the maximum value. Figure 9b also suggests that the elastic approximation defined by equation (17) overestimates the values of radial displacements when compared with the measured data at the Mingtam Power Cavern project and with the statistical approximation to this data. As seen in Figure 3, this overestimation results in underestimation of the final load transmitted to the support.

Ideally, for tunnels designed according to the Convergence-Confinement method, the LDP should be constructed from measured data such as the one presented by Chern et al. (1998). Where such information is not available, the LDP can be constructed from numerical models considering the same elasto-plastic parameters used in construction of the Ground Reaction Curve. Alternatively, and as a first approximation, the LDP could be evaluated using relationship (18).

6. Example

To illustrate the application of the Convergence-Confinement method in the design of tunnel supports we will re-examine the case of the circular tunnel of radius R =1 m shown in Figure 4a. The uniform far-field stress acting in

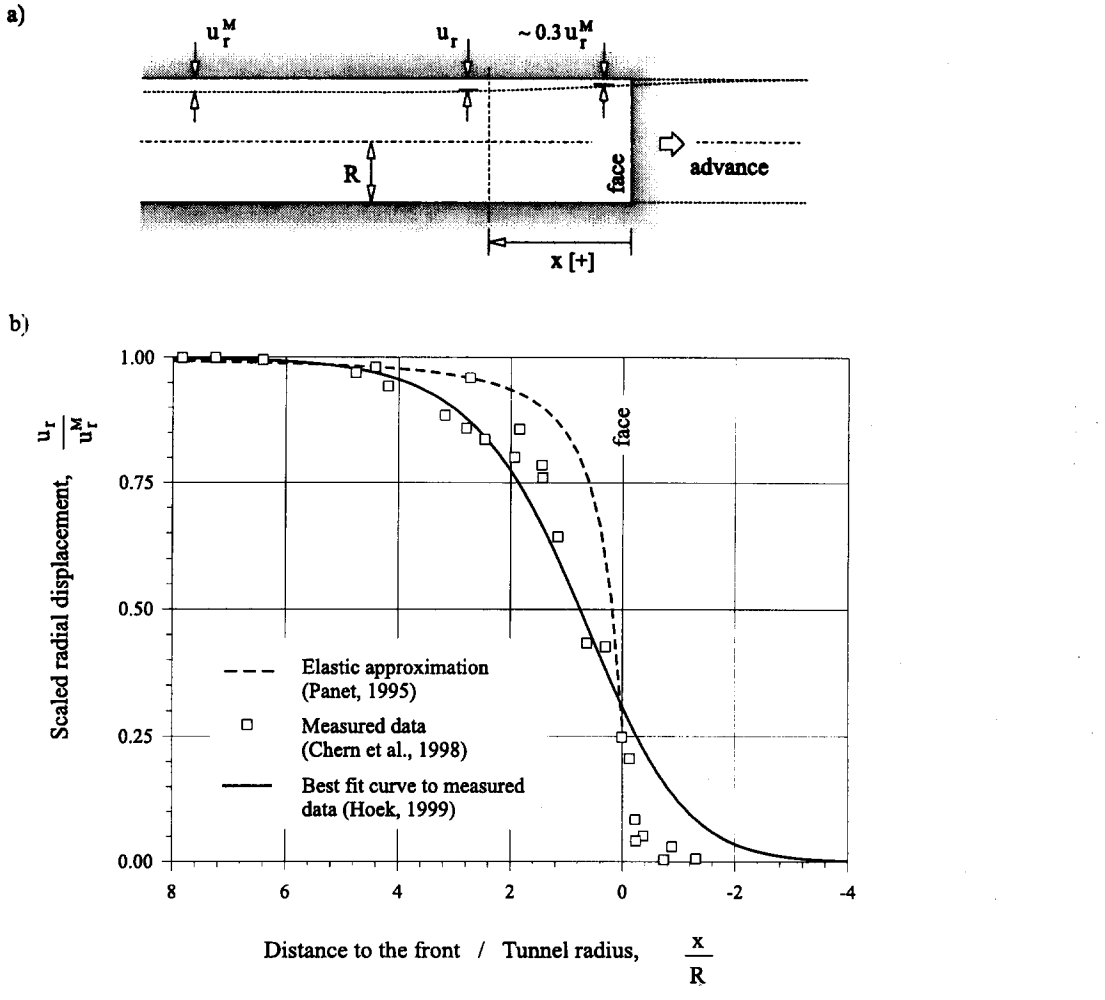

Figure 9. a) Profile of radial displacements u_r for an unsupported tunnel in the vicinity of the tunnel face. b) Deformation profiles derived from elastic models (Panet 1995); measurements in a tunnel (Chern et al. 1998); and best fit to the measurements (Hoek 1999).

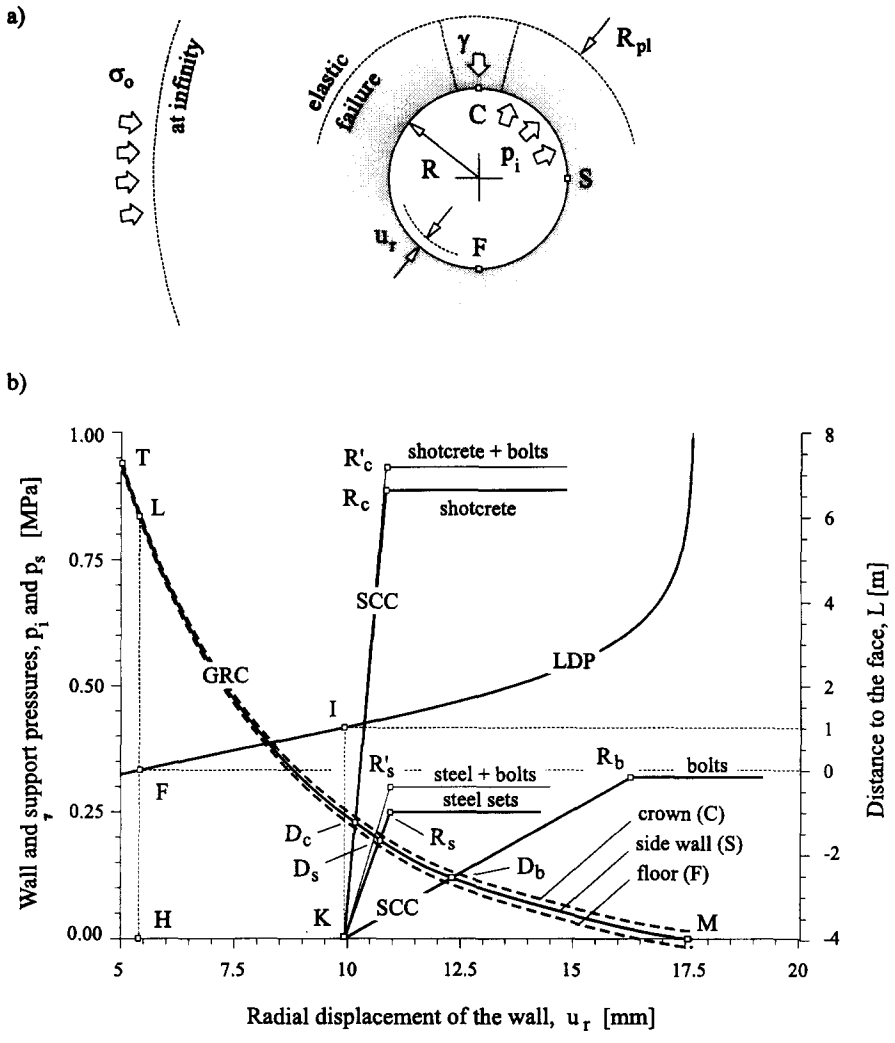

Figure 10. a) Influence of the weight of failed rock in the crown and the floor of a tunnel on the Ground Reaction Curve (points C and F, respectively). b) Rock-support interaction analysis for the tunnel shown in Figure 4 and the support systems shown in Figure 8.

the rock-mass is σ_o =7.5 MPa. A Geological Strength Index equal to 40 is assumed for the rock. The properties of the rock-mass are as indicated in the diagram.

We wish to assess the mechanical behavior of the different support systems considered in Figure 8, assuming that the supports are installed at a distance L=1 m behind the face of the tunnel.

Solution of this problem requires application of the equations presented in Sections 3, 4 and 5, for construction of the GRC, SCC and LDP respectively. Appendix C includes the outline of a spreadsheet for ease in implementation of the equations and construction of the GRC, SCC and LDP. The results of the example are summarized in Figure 10.

For the problem being considered, the GRC is the curve identified as *GSI* = 40 in Figure 4b. In defining the GRC for a tunnel, it is usual to distinguish between the convergence of side wall, roof and floor of the tunnel (Daemen 1975), since gravitational loading differs for each of these points around the tunnel periphery. The GRC shown in Figure 4b (the curve corresponding to *GSI* = 40) is considered to be representative of the load-convergence relationship for a point on the side-wall of the tunnel—point S in Figure 10a. For the same internal pressure p_i, the convergence of the roof can be expected to be larger than that at the side because of the weight of the failed material on top of the tunnel (point C in the figure). The GRC for the roof can then be obtained by adding the same amount $\gamma\,(R_{pl}-R)$ to the internal pressure p_i, where γ is the unit weight of the rock-mass and R_{pl} is the extent of the plastic region —values of γ for different rock types are listed in Table A-1. Similarly, the GRC for the floor of the tunnel can be obtained by subtracting the amount $\gamma(R_{pl}-R)$ from the internal pressure p_i (see point F in Figure 10a).

Figure 10b shows an enlargement of the diagram of Figure 4b, representing the GRC curve for *GSI* = 40. The solid curve that extends from point *T* to point *M* represents the radial displacement of point S in Figure 10a. The dotted curves above and below this curve are the GRC's for the crown (point C) and floor (point F) for an assumed rock-mass unit weight γ =24 × 10^{-3} MN/m³. Note that the pressure transmitted at the crown of the tunnel is slightly higher than the pressure at the floor.

The LDP computed from equation (18) is also shown in Figure 10b. This curve is an enlargement of the solid curve in Figure 9b (note that, in Figure 10b, the distance to the face is shown on the vertical axis on the right side, and the associated

radial displacement on the horizontal axis). For the distance L = 1 m between the face and the support at installation, the LDP allows to define the point K (horizontal coordinate $u_r \approx 10$ mm), from which the SCC starts (see also point K, Fig. 3). In Figure 10, the face of the tunnel is identified by the vertical line passing through point F, that is defined by the coordinate L = 0 m in the vertical axis on the right.

The SCC for the support systems shown in Figure 8 are also represented in Figure 10b. Note that only shotcrete (30 mm thick), steel sets and bolts are considered as support alternatives in this problem. The SCC for the combination of two support systems (shotcrete and bolts *and* steel sets and bolts) are also shown in the figure.

Following the notation in Figure 3, the maximum stress p_s^{max} for each of the different support systems is indicated as points R and R' (for the individual and the combined systems, respectively). For example, the maximum support pressure for steel sets is ≈ 0.25 MPa, for steel sets and bolts ≈ 0.30 MPa, for bolts ≈ 0.35 MPa, for shotcrete ≈ 0.88 MPa, and for shotcrete and bolts ≈ 0.94 MPa.

As mentioned above, the point K is defined by the LDP for a distance to the face of L = 1 m. It is evident from this diagram, that the point K cannot lie to the left of point H, which represents the face of the tunnel. Therefore, the maximum possible pressure that the rock-mass can transmit to any given support in this problem will be less than the pressure defined by the vertical coordinate of point L in the figure —this is ≈ 0.84 MPa (see Section 2).

Points D_s, D_c and D_b in Figure 10 represent the final support pressure that the rock-mass will transmit to the different support systems, once the tunnel face has moved well away from the support; for example, the final pressure transmitted by the rock-mass is ≈ 0.12 MPa for bolts (D_b); ≈ 0.20 MPa for steel sets (D_s) and ≈ 0.23 MPa for shotcrete (D_c).

Analysis of the location of points D in the diagram indicates that all the supports considered in this problem are capable of sustaining the final load transmitted by the rock-mass (note that points D lie below the corresponding 'support-capacity' points R). The relative merits of one or other of the support systems will depend on the allowable amount of convergence and/or the value of safety margin against failure desired for the support.

The final convergence for each support system is given by the horizontal coordinate of the various points D; for example, for shotcrete the convergence is ≈ 10.1 mm, for steel sets ≈ 10.6 mm and for bolts ≈ 12.4 mm.

The safety coefficients for the different supports can be obtained as the ratio between the vertical coordinates of points R and D in the figure; for example, for bolts the ratio is 0.30/0.12 [MPa/MPa], indicating a safety coefficient of ≈ 2.5. If minimizing the wall closure is a primary concern, the steel sets and shotcrete are the best alternative (note that the horizontal coordinate of point D_b is significantly larger than the horizontal coordinates of points D_c or D_s). On the other hand, if a large safety coefficient is desired, shotcrete and bolts are superior to steel sets (note that the ratio of vertical coordinates of points R_s and D_s is significantly lower than those for points R_c and D_c and R_b and D_b). If steel sets are required to be used to line the tunnel anyway, it may be worth considering installation of bolts in combination with the sets. This is justified by the significant improvement of the 'safety' margin —i.e., the ratio of vertical coordinates of points R_s and D_s (≈ 0.25/0.20 = 1.25) compared to R'_s and D_s (≈ 0.30/0.20 = 1.5).

7. Limits of Application of the Convergence-Confinement Method

The Convergence-Confinement method is based on two important assumptions:

i) the far-field principal stresses normal to the long axis of the tunnel are of constant magnitude σ_o, independent of the radial orientation (such a state of stress is often referred to as *uniform* or *hydrostatic*); and

ii) the tunnel cross-section is circular, of radius R.

This section discusses the validity of the method for cases in which the far-field (principal) stresses are unequal and the tunnel cross-section is non-circular.

The principal stresses that exist at the site prior to excavation of a tunnel depend on the geological history of the site and in general are unequal. Figure 11a, adapted from Hoek and Brown (1980), shows measured values of vertical stresses σ_z as a function of depth z for different regions of the world. The linear function that best fits the measured data is given by the relationship,

$$\sigma_z = 0.027\, z \qquad (19)$$

where σ_z is expressed in MPa and z in meters. If the vertical stress at a depth z is assumed to be associated with the weight of overburden material (i.e., the lithostatic pressure at the depth z), equation (19) suggests that the mean unit weight of the rock where the measurements were made is about 0.027 MN/m^3. This value corresponds to the unit weight of silicates, a major component of many rocks (see Table A-1).

The mean horizontal stress σ_x at a depth z is usually expressed in terms of the corresponding vertical stress σ_z. The horizontal-to-vertical stress ratio k (also referred to in soil mechanics as the 'at-rest' coefficient of earth pressure) is defined as

$$k = \frac{\sigma_x}{\sigma_z} \qquad (20)$$

Figure 11b, adapted from Hoek and Brown (1980), shows the values of the coefficient k corresponding to the vertical stresses in Figure 11a. The diagram indicates that the horizontal stresses σ_x are bounded by the two curves shown. The *minimum* value of mean horizontal stress is ≈ 0.5 times the value of vertical stress and the *maximum* value of horizontal stress is ≈ 3.5 times the mean value of vertical stress. Even higher ratios than those indicated in Figure 11b have been recorded. At the Underground Research Laboratory (URL) in Pinawa (Canada), for example, the mean horizontal stress in the Lac du Bonnet granite is 52 MPa, at a depth of 420 m —with a vertical stress of approximately 11 MPa, i.e., k = 4.6 (see Martin and Simmons 1993).

The diagrams in Figure 11 suggest that the principal stresses at the site are often unequal. They also indicate that the vertical stress will probably vary with depth according to a lithostatic gradient.

If the dimensions of the cross section of the tunnel are small compared to the depth z of the tunnel, the far-field stresses σ_z and σ_x can be assumed to be constant over the proposed tunnel section (e.g., the vertical in-situ stress at the depth of the crown and invert of the proposed tunnel can be considered to be the same —and similarly for the horizontal in-situ stresses).

Two quantities can be used to characterize a given non-uniform plane stress state (σ_x, σ_z): the dimensionless coefficient k—defined by equation (20), and the mean stress σ_o defined as

$$\sigma_o = \frac{\sigma_x + \sigma_z}{2} \qquad (21)$$

The uniform state of stress assumed by the Convergence-Confinement method can be expressed as $\sigma_o = \sigma_z = \sigma_x$ and $k = \sigma_x / \sigma_z = 1$ (see Fig. 1b).

The elasto-plastic problem of excavating a circular tunnel in a non-uniform stress field has been studied analytically by a few investigators.

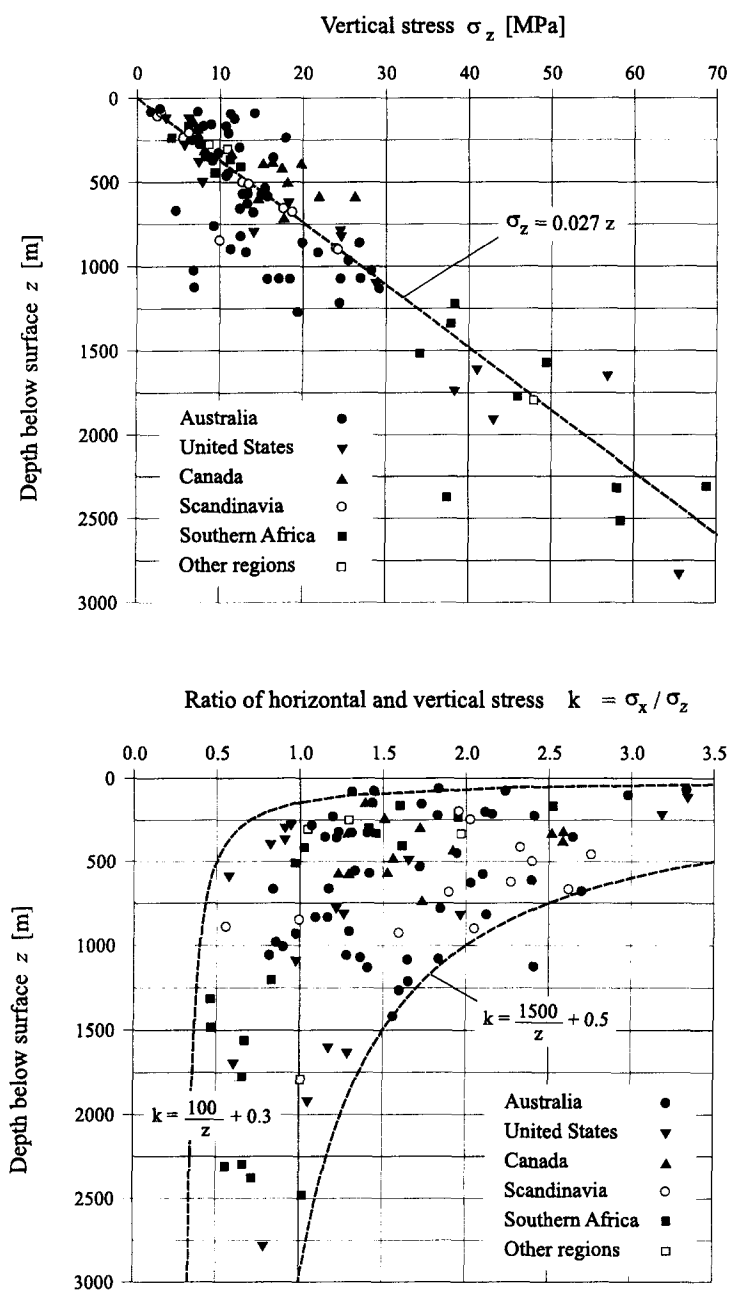

Figure 11. a) Measured values of vertical stress σ_z as a function of depth z in different regions of the world. b) Corresponding values of horizontal-to-vertical stress ratio k (adapted from Hoek and Brown 1980).

Detournay and Fairhurst (1987) considered the case of a circular cavity subject to unequal far-field stresses and excavated in a Mohr-Coulomb material. Figure 12a illustrates the problem considered. A circular cavity of radius R is subject to a uniform internal pressure p_i and horizontal and vertical stresses σ_x and σ_z, respectively; the figure considers the case $\sigma_x > \sigma_z$ (because of the symmetry of the problem, the case $\sigma_x < \sigma_z$ can be obtained by rotating the axes of the cavity through 90°).

In contrast to the Hoek-Brown failure criterion (A-2) discussed in Appendix A, the Mohr-Coulomb failure criterion considered by Detournay and Fairhurst is

$$\sigma_1 = K_p\, \sigma_3 + \sigma_{ci} \qquad (22)$$

where σ_{ci} is the unconfined compressive strength of the intact rock and K_p is the 'passive reaction' coefficient that is computed from the friction angle ϕ of the intact rock as

$$K_p = \frac{1 + \sin\phi}{1 - \sin\phi} \qquad (23)$$

It was found that, when the stress state represented in Figure 12a is expressed in terms of the parameters σ_o and k defined by equations (21) and (20), respectively, cavities with horizontal-to-vertical stress coefficients k smaller than a limiting value k_{lim} are statically determinate. The authors also made the interesting observation that the mean radius of the plastic region around the tunnel and the mean convergence at the crown and sidewall of the tunnel are the same as the corresponding values for a cavity subject to *hydrostatic* far-field stresses σ_o —i.e., comparing Figures 1b and 12a, $R_{pl} \approx 0.5\,(R_{pl1} + R_{pl2})$ and $u_r \approx 0.5\,(u_{r1} + u_{r1})$. Cavities with a horizontal-to-vertical stress coefficient k larger than a limiting value k_{lim}, are statically indeterminate and develop a 'butterfly-shaped' failure zone (see Figure 12a); for these cases, the extent of the failure zone and the displacements around the periphery of the tunnel are decidedly non-uniform —and have no apparent relationship to the case of uniform loading σ_o represented in Figure 1b.

The limiting coefficient k_{lim} can be determined from the values of scaled mean pressure σ_o / σ_{ci} and friction angle ϕ in Figure 12b. Note that the diagram in Figure 12b assumes that the cavity is unsupported. Because of the self-similar nature of the problem, the diagram also applies to cases in which there is a uniform internal pressure acting inside the cavity. In such cases, the value of k_{lim} is read from Figure 12b by taking an equivalent ratio of mean pressure and compressive strength $\sigma_o / \sigma_{ci}\,|_{eq}$, as given by the expression in equation (24), (after Detournay and St. John 1988),

$$\left.\frac{\sigma_o}{\sigma_{ci}}\right|_{eq} = \frac{\frac{\sigma_o}{\sigma_{ci}}\left(1 - \frac{p_i}{\sigma_o}\right)}{\frac{p_i}{\sigma_o}\frac{\sigma_o}{\sigma_{ci}}\left(K_p - 1\right) + 1} \qquad (24)$$

Figure 12b can be used to evaluate the applicability of the Convergence Confinement method when the far-field stresses are non-uniform. For tunnels characterized by coefficients k smaller than the value k_{lim} shown in the figure, the Convergence-Confinement method provides a reasonable estimation of the shape of the failure zone and displacements to expect around the cavity. For tunnels characterized by coefficients k larger than the value k_{lim} shown in the figure, the resulting shape and extent of the failure zone and the convergence around the tunnel will be too variable to apply the method. For these cases, numerical analysis should be used for the design.

As mentioned above, Figure 12b applies to Mohr-Coulomb materials characterized by a friction angle ϕ and unconfined compressive strength σ_{ci} (and linear failure envelope). For Hoek-Brown materials considered in this study, an equivalent diagram to that represented in Figure 12b could be constructed by approximating the Hoek-Brown

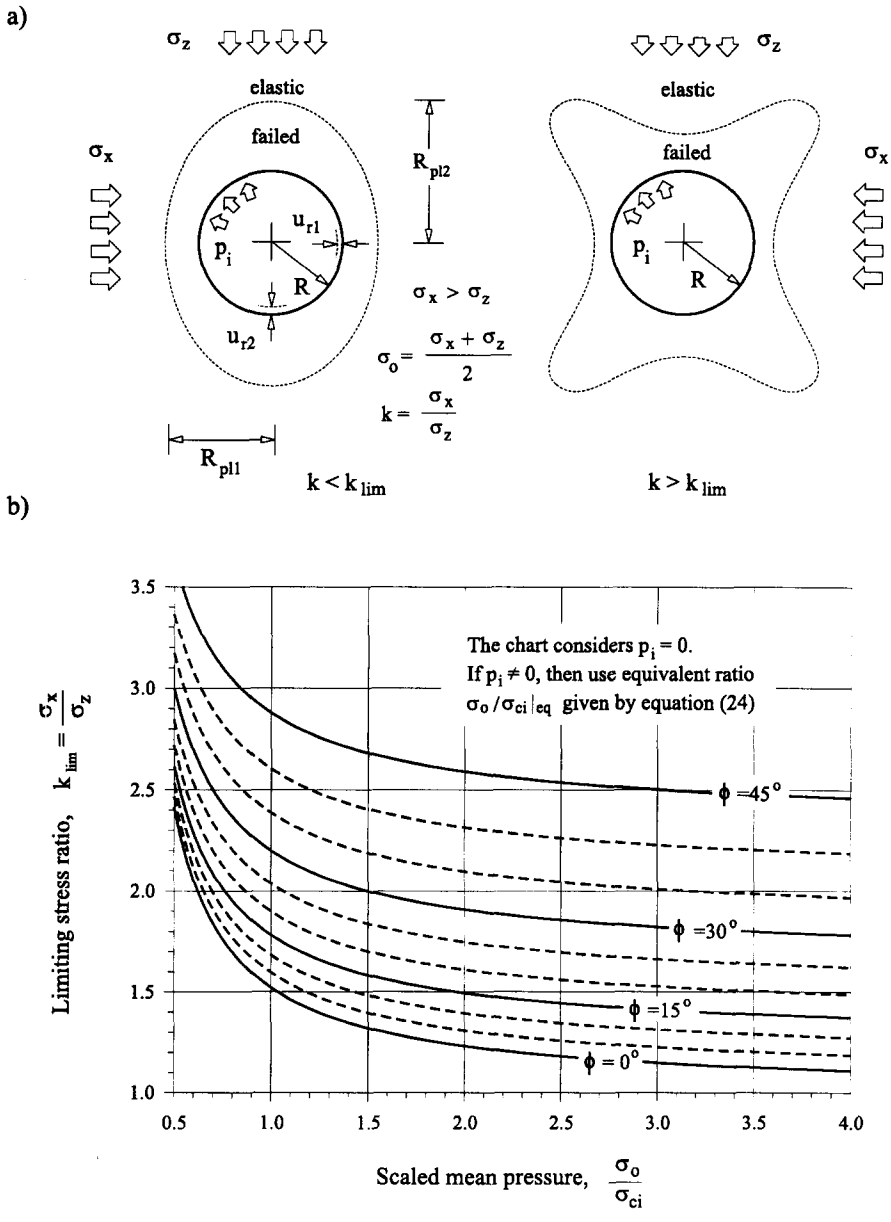

Figure 12. a) Circular cavity in a Mohr-Coulomb material subject to uniform internal pressure and unequal far-field stresses. b) Limiting values of the horizontal-to-vertical stress ratio k_{lim} as a function of the scaled mean stress σ_o / σ_{ci} and friction angle ϕ. For $k < k_{lim}$, the problem is statically determinate, and the mean values of failure extent and wall closure are comparable to those obtained for uniform loading σ_o and k=1 (adapted from Detournay and Fairhurst 1987).

parabolas of Figure A-1 as straight lines with 'equivalent' friction angle ϕ and unconfined compressive strength σ_{ci} (examples of this type of approximation can be found in Hoek 1990).

For tunnels driven in Hoek-Brown materials under unequal far-field stresses, an indication of the expected shape of the failure zone —and thus an estimate of the applicability of the Convergence-Confinement method, can be obtained from elastic analysis. Figure 13a presents the results from an analysis of this type. The different curves in the figure represent the extent of the 'over-stressed' regions determined by comparing the maximum and minimum elastic stresses at a point as given by the Kirsch elastic solution, with the Hoek-Brown strength criterion (A-2), i.e.,

$$\sigma_1 \geq \sigma_3 + \sigma_{ci} \left(m_b \frac{\sigma_3}{\sigma_{ci}} + s \right)^a \qquad (25)$$

If the elastic stresses exceed the strength indicated by equation (25), the rock at that point is *over-stressed*. The diagrams in Figure 13a show cases of unequal far-field stresses characterized by σ_o=7.5 MPa and different values of horizontal-to-vertical stress ratio k, together with rock-mass strength parameters σ_{ci}=20 MPa, m_b=1.8 and s =1.3 $\times 10^{-3}$ in the yield criterion (25). The curves on the right side of the diagram correspond to horizontal-to-vertical stress coefficients $k < 1$ and the curves on the left side of the diagram to coefficients $k > 1$. The equations and a spreadsheet needed to construct these curves are shown in Appendix D. It is seen, for example, that for $k < 0.6$, the *over-stressed* region has the 'butterfly' shape discussed in the analysis by Detournay and Fairhurst. The Convergence-

Confinement method should not be used for such cases. Elastic rock-support interaction analyses such as those presented by Einstein and Schwartz (1979) and Matsumoto and Nishioka (1991) are preferable in these cases. Wherever possible, results obtained from these elastic analyses should be verified against results obtained from elasto-plastic numerical analyses. The latter consider stress and displacement changes that occur due to formation of the plastic zone.

However, although approximate, the shape of the plastic zone obtained from the elastic *over-stressed* analysis is generally comparable to the correct one (note that the *extent* of the plastic or failed zone, can be considerably underestimated by this approach). For example, Shen and Barton (1997) have used the elastically *over-stressed* zone concept to identify the shape of regions where shear failure is likely to occur in heavily jointed rock-masses. They showed that the shape of the regions of 'slipping' joints derived from elastic analysis was comparable to the shape obtained using the discrete element numerical model UDEC (Cundall 1971).

Figure 13b shows a *FLAC*^{3D} elasto-plastic model of the problem shown in Figure 4; the elasto-plastic model considers the far-field stresses to be σ_z =10.3 MPa and σ_x =4.7 MPa (i.e., σ_o = 7.5 MPa and k = 0.45). It is seen that the shape of the resulting failure zone in the *FLAC*^{3D} model is comparable to the shape given by the curve corresponding to k = 0.45 in Figure 13a.

The assumption of circular cross-section of the tunnel in combination with hydrostatic far-field stresses guarantees that the displacements around the tunnel will be constant all around the periphery. In practical design of tunnels, the actual cross-section depends mainly on the purpose of the tunnel. For example, Figure 14a shows a 'horseshoe' shape chosen for a motorway tunnel in Germany. The width and height of the cross section depend on the number of lanes and maximum height of vehicles that the tunnel needs to serve.

For cases in which the cross-sectional area of the tunnel is not circular, the Convergence-Confinement method can still be used to provide a first estimate of the extent of the failure zone and the resulting convergence of the walls. Within certain limits, the shape of the tunnel can be regarded as circular with a radius equal to the mean value of the maximum and minimum dimensions of the section. In such cases, the mean extent of the failure zone and the mean convergence at the walls for the non-circular geometries are comparable to the values one would predict for the equivalent circular section.

Figure 14 shows the results of a 3DEC (Itasca Consulting Group 1998a) elasto-plastic analysis of the cross-sectional area shown in Figure 14a for the stress conditions and rock-mass and support properties indicated in the figure. Application of the Convergence-Confinement method assuming the section to be circular of radius R = 4 m, leads to a plastic zone R_{pl} ≈ 6 m in extent. It is seen that this extent is comparable with that obtained from the 3DEC model in which the actual geometry of the cross-section is considered. Results for the loads and the convergence in the lining are also comparable.

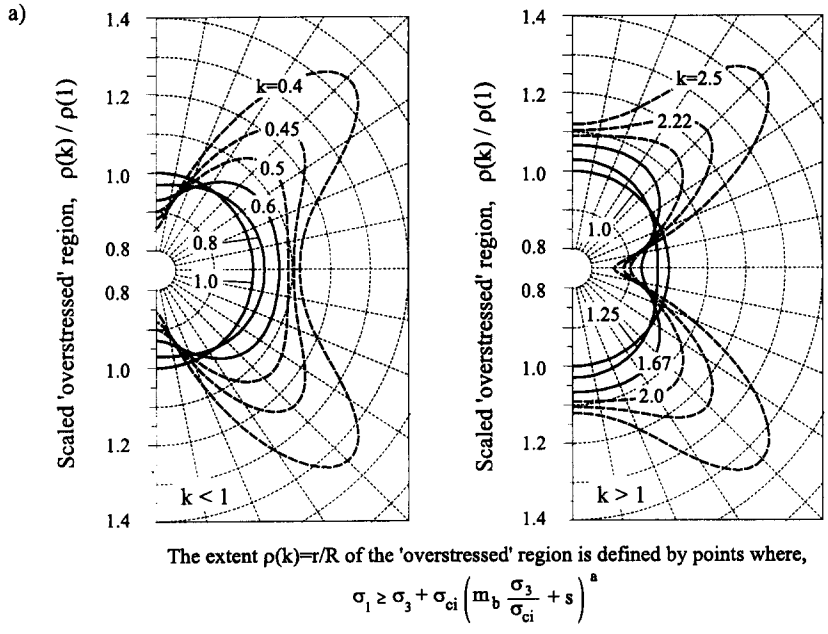

b)

R = 1 m
σ_x = 4.65 MPa
σ_z = 10.34 MPa
σ_o = 7.5 MPa
k = 0.45

σ_{ci} = 20 MPa
m_i = 15
GSI = 40
m_b = 1.8
s = 1.3 x 10^{-3}

G_{rm} = 1.0 GPa
ν = 0.25
ψ = 30°

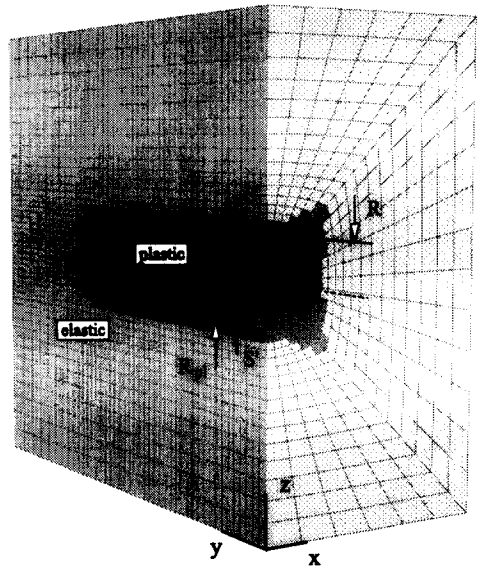

Figure 13. a) Diagrams indicating the extent of the elastically 'over-stressed' regions computed from the elastic analysis of a circular cavity subject to non-hydrostatic loading; the charts are valid for ratios $m_b\,\sigma_{ci}\,/\,\sigma_o = 4.8$ and $s/m_b^2 = 4 \times 10^{-4}$. For example, when σ_o=7.5 MPa, σ_{ci}=20 MPa, m_b=1.8 and $s = 1.3 \times 10^{-3}$ (see Appendix D). b) FLAC^{3D} *elasto-plastic analysis of the problem represented in Figure 4 for highly unequal far-field principal stresses.*

8. Discussion

The Hoek-Brown criterion and its scaled form discussed in Appendix A is a convenient and widely used method for describing the strength of rock-masses in situ. When applying the criterion to real cases, the engineer should bear in mind the limitations, pointed out by Hoek and Brown in deriving the criterion. Probably the most important of these is the assumption of elastic

perfectly-plastic isotropic behavior for the material. If the rock-mass contains joints with a preferred orientation, the mechanical behavior can be expected to be anisotropic and the Hoek-Brown criterion may give quite misleading results. In such cases, a treatment with elasto plastic non-isotropic models (such as the ubiquitous joint model implemented in the continuum code *FLAC*) or with discontinuum models (such as *UDEC*) would be more appropriate (Itasca 1996, 1998).

In cases where the rock-mass is reasonably well described as isotropic, such that the Hoek-Brown criterion can be applied with reasonable confidence, the Convergence-Confinement method described in this paper can be used to obtain a useful estimate of the magnitude of loads that the rock-mass will transmit to supports installed behind the face of a tunnel.

As discussed in Section 2, the Convergence-Confinement method relies on several simplifying assumptions, the most important of which are the circular geometry of the tunnel and hydrostatic (or uniform) far-field stresses. In this case, the loads transmitted by the rock-mass to the support are uniform within each section. If the geometry of the tunnel is non-circular or the far-field stresses are non-uniform, the loads will not be uniform and bending moments will be induced in the support.

For situations in which the assumptions mentioned above are violated, the Convergence-Confinement method is still useful in the early stages of the design. As discussed in Section 7, a characteristic tunnel radius and a characteristic uniform stress can be computed from the existing geometry and far-field stresses and the engineer can then make quick comparisons of the mechanical response of different support alternatives—under representative conditions of rock-mass deformability and strength. This can help in deciding on the most convenient support system in the actual case. The final design of the support—which would probably require consideration of the distribution of bending moments and compressive loads induced by the non-uniform far-field stresses— can be made later on the basis of more rigorous numerical analyses of the rock-support interaction problem.

In summary, the Convergence-Confinement method is a useful tool not only for the design of supports in tunnels, but also as a simple illustrative model that allows a better understanding of the complex problem of transference of loads in the vicinity of the tunnel face.

References

AFTES, French Association for Underground Works. (1978). Analysis of tunnel stability by the Convergence-Confinement Method. *Underground Space* **4** (4), 221—223.

Atkinson, J. (1993). *An Introduction to the Mechanics of Soils and Foundations.* New York: McGraw-Hill Book Company.

Bieniawski, Z.T. (1976). Rock mass classification in rock engineering. In Bieniawski (Ed.), *Proc. of the Symp. in Exploration for Rock Engineering, Cape Town*, 97-106. Rotterdam: Balkema.

Brady, B.G.H. and E.T. Brown (1985). *Rock Mechanics for Underground Mining* (Second ed.). New York: Chapman & Hall.

Brown, E.T., J.W. Bray, B. Landayi, and E. Hoek (1983). Ground response curves for rock tunnels. *ASCE J. Geotech. Eng. Div.* **109** (1), 15–39.

Carranza-Torres, C. and C. Fairhurst (1999). The elasto-plastic response of underground excavations in rock masses that satisfy the Hoek-Brown failure criterion. *Int. J. Rock Mech. Min. Sci.* **36** (6), 777–809.

Chern, J.C., F.Y. Shiao, and C.W. Yu (1998). An empirical safety criterion for tunnel construction. In *Proc. Regional Symposium on Sedimentary Rock Engineering, Taipei, Taiwan*, 222–227.

CONSTRADO. 1983. *Steel Designers' Manual*. Granada: Constructional and Steel Research and Development Organisation.

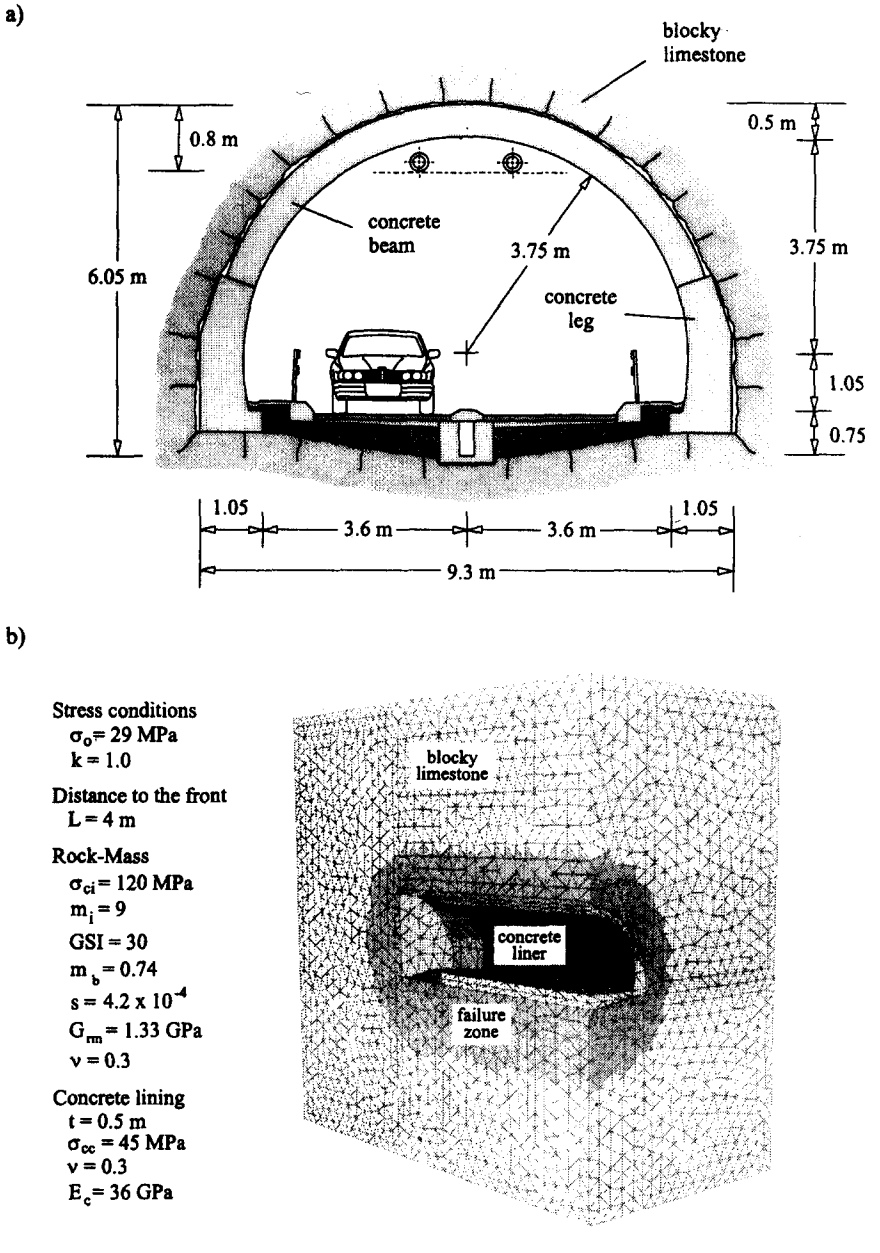

Figure 14. a) Cross-section of a German motorway tunnel in 'hydrostatically' loaded rock. b) 3DEC elasto-plastic model of the rock-support interaction problem. The extent of the failure zone predicted numerically is seen to agree with the value obtained from the Convergence-Confinement method; i.e., in this case, it is ≈ 1.5 times the characteristic radius of the tunnel.

Cundall, P.A. (1971). A computer model for simulating progressive large movements in blocky rock systems. *Proceedings of the Symposium of the International Society of Rock Mechanics, Volume 1,* Paper No. II-8.
Daemen, J. J. K. (1975). *Tunnel support loading caused by rock failure*. Ph. D. thesis, University of Minnesota.
Derucher, K. and G. Korfiatis (1988). *Materials for Civil and Highway Engineers.* New York: Prentice Hall.
Detournay, E. and C. Fairhurst (1987). Two-dimensional elasto-plastic analysis of a long, cylindrical cavity under non-hydrostatic loading. *Int. J. Rock Mech. Min. Sci. & Geomech. Abstr.* **24** (4), 197–211.
Detournay, E. and C. St. John (1988). Design charts for a deep circular tunnel under non-uniform loading. *Rock Mechanics and Rock Engineering* **21**, 119–137.
Dodge, M., C.Kinata, and C.Stinson (1997). *Running Microsoft Excel 97*. Redmond. Washington: Microsoft Press.
Einstein, H.H. and C.W. Schwartz (1979). Simplified analysis for tunnel supports. *ASCE J. Geotech. Eng. Div.* **104** (4), 499—518.
Fenner, R. (1938). Untersuchungen zur Erkenntnis des Gebirgsdruckes. *Glückauf* **74**, 681-695 and 705-715.
Franklin, J. A. and E. Hoek (1970). Developments in triaxial testing technique. *Rock Mechanics* **2**, 223–228.
Gieck, K. (1977). *Technische Formelsammlung*. Berlin: Verlag.
Goodman, R. E. (1980). *Introduction to Rock Mechanics.* New York: Wiley and Sons.
Hoek, E. (1983). Strength of jointed rock masses. Rankine Lecture. *Geotechnique* **33** (3), 187–223.
Hoek, E. (1990). Estimating Mohr-Coulomb friction and cohesion values from the Hoek-Brown failure criterion. *Int. J. Rock Mech. Min. Sci. & Geomech. Abstr.* **27** (3), 227–229.
Hoek, E. (1999). Personal communication.
Hoek, E. and E. T. Brown (1980). *Underground Excavations in Rock.* London: The Institute of Mining and Metallurgy.
Hoek, E. and E. T. Brown (1997). Practical estimates of rock mass strength. *Int. J. Rock Mech. Min. Sci. & Geomech. Abstr.* **34** (8), 1165–1186.
Hoek, E., P. K. Kaiser, and W. F. Bawden (1995). *Support of Underground Excavations in Hard Rock.* Rotterdam: Balkema.
Hoek, E., P. Marinos, and M. Benissi (1998). Applicability of the Geological Strength Index (GSI) classification for very weak and sheared rock masses. The case of the Athens Schist Formation. *Bull. Eng. Geol. Env.* **57** (2), 151–160.
Itasca Consulting Group (1996). *UDEC. Universal Distinct Element Code. Version 3.0.* User Manual. Minneapolis: Itasca.
Itasca Consulting Group (1997). *FLAC^{3D}. Fast Lagrangian Analysis of Continua in 3 Dimensions.* Version 2.0. User Manual. Minneapolis: Itasca.
Itasca Consulting Group (1998a). *3DEC. 3 Dimensional Distinct Element Code. Version 2.0.* User Manual. Minneapolis: Itasca.
Itasca Consulting Group (1998b). *FLAC. Fast Lagrangian Analysis of Continua. Version 3.4.* User Manual. Minneapolis: Itasca.
Jaeger, J.C. and N.G.W. Cook (1979). *Fundamentals of rock mechanics* (Third ed.). New York: John Wiley & Sons.
Labasse, H. (1949). Les pressions de terrains dans les mines de huiles. *Revue Universelle des Mines*, Liège, Belgium, Series 9, Vol. 5, No. 3, 78–88.
Lama, R.D. and V.S. Vutukuri (1978). *Handbook of Mechanical Properties of Rocks. Testing Techniques and Results. Volume II.* Trans Tech Publications.
Leonhardt, F. (1973). *Vorlesungen über Massivbau.* Berlin: Springer-Verlag.
Londe, P. (1988). Discussion on the determination of the shear stress failure in rock masses. *ASCE J. Geotech. Eng. Div.* **114**(3), 374–376.
Martin, C.D. and G.R. Simmons (1993). The Atomic Energy of Canada Limited Underground Research Laboratory: An Overview of Geomechanics Characterization. In J.A. Hudson (Ed.), *Comprehensive Rock Engineering*, 915–950. Pergamon: Oxford.
Matsumoto, Y. and T.Nishioka (1991). *Theoretical Tunnel Mechanics.* Tokyo: University of Tokyo Press.
Panet, M. (1995). *Calcul des Tunnels par la Méthode de Convergence-Confinement.* Paris: Press de l'école Nationale des Ponts et Chaussées.
Serafim, J.L. and J.P. Pereira (1983). Consideration of the geomechanical classification of Bieniawski. In *Proc. Int. Symp. on Engineering Geology and Underground Construction. Lisbon, Volume 1 (II)*, 33–44.
Shen, B. and N.Barton (1997). The disturbed zone around tunnels in jointed rock masses. *Int. J. Rock Mech. Min. Sci. & Geomech. Abstr.* **34** (1), 117–125.
Singh, M.M. and S.A. Bortz (1975). Use of special cements in shotcrete. In *Use of Shotcrete for Underground Structural Support*, 200–231. New York: American Society of Civil Engineers.
Stillborg, B. (1994). *Professional Users Handbook for Rock Bolting.* Trans Tech Publications.
Timoshenko, S.P. and J.N. Goodier (1970). *Theory of Elasticity* (Third ed.). New York: McGraw Hill.
Wang, Y. (1996). Ground response of a circular tunnel in poorly consolidated rock. *ASCE J. Geotech. Eng.* **9**, 703–708.

Appendix A. The strength and deformability of rock-masses according to the Hoek-Brown failure criterion.

The Hoek-Brown criterion has found wide practical application as a method of defining the stress conditions under which a rock-mass will deform inelastically and, if not supported adequately, collapse.

The parameters defining the Hoek-Brown criterion can be estimated from a combination of laboratory tests on intact rock cores and an empirical 'adjustment' to account for the reduced strength of the rock-mass due to the presence of weaknesses and jointing.

It must be noted that this criterion assumes continuum-isotropic behavior for the rock-mass and should not be applied to cases in which there is a preferred orientation of jointing, such that the mass would not behave as an isotropic continuum.

Testing of rock specimens under triaxial conditions of loading allows the combination of stresses that lead to failure (or collapse) of the specimen to be determined. According to Hoek and Brown, the failure condition of *intact rock* samples is given by the following parabolic law (Hoek and Brown 1980),

$$\sigma_1 = \sigma_3 + \sigma_{ci}\sqrt{m_i \frac{\sigma_3}{\sigma_{ci}} + 1} \qquad \text{(A-1)}$$

where

- σ_3 is the confining stress applied to the sample (e.g., in MPa);
- σ_1 is the axial stress that produces failure of the sample (e.g., in MPa);
- σ_{ci} is the unconfined compression strength of the intact rock (in MPa);
- m_i is a dimensionless parameter, the value of which depends on the type of rock being tested.

In order to characterize the intact rock in terms of equation (A-1), it is necessary to determine the parameters σ_{ci} and m_i. This is done by statistical analysis of strength σ_1 observed for various values of confining stress σ_3 in triaxial tests (Hoek 1983). Appendix B explains this procedure and lists the equations needed to perform the analysis.

To illustrate the application of equation (A-1), let us consider the triaxial test results shown in Figure A-1 obtained by Franklin and Hoek (1970) for samples of different rock types: *i)* granite, *ii)* quartz dolerite and *iii)* marble (details of the tests can be found in the original paper; Appendix B shows a summary only of the results).

The horizontal and vertical axes in the diagram correspond, respectively, to the confining stress σ_3 and the axial stress at failure σ_1 divided by the unconfined compression strength σ_{ci} for each rock type. The dots represent the pairs (σ_3, σ_1) obtained from the triaxial tests (see Appendix B). The solid lines are the corresponding failure envelopes defined by equation (A-1) with the parameters σ_{ci} and m_i computed from equations (B-1) and (B-2) in Appendix B. It can be seen that, although there is some dispersion in the results, the general trend is for the scattered points to align to the parabolas defined by equation (A-1) [a].

Triaxial testing of rock samples is an expensive procedure and, in most cases, results of the extensive tests needed to determine the parameters σ_{ci} and m_i in the relationship (A-1) are not available. In this case, when information on the unconfined compressive strength is available (e.g., from UCS tests or, indirectly, from Point Load Tests), the parameter m_i may be estimated from empirical charts or tables (Hoek et al. 1995).

Table A-1 and Figure A-2, adapted from Lama and Vutukuri (1978), Goodman (1980) and Hoek and Brown (1997), respectively, show typical values of σ_{ci} and m_i for different rock types that could be taken as a reference for use in equation (A-1).

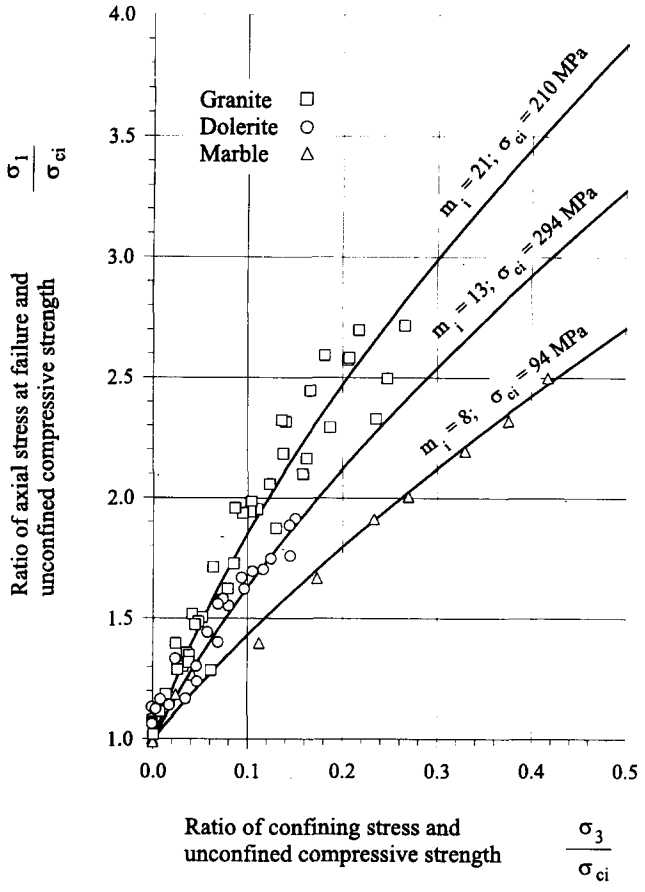

Figure A-1. Failure envelopes obtained from triaxial tests of samples of different rock types (after Franklin and Hoek 1970). The horizontal and vertical axes represent the confining stress σ_3 and the maximum axial stress σ_1 respectively divided by the unconfined compressive strength σ_{ci} of the sample (see Appendix B).

As noted earlier, joints and defects in a rock-mass reduce the strength of the mass below the strength of an intact specimen of the same rock type. By using the so-called *Geological Strength Index* (or *GSI*) as a scaling parameter, the failure criterion defined by equation (A-1) can be adjusted to provide an estimate of the decreased strength of the rock-mass in the field.

According to Hoek and Brown (1997), the GSI is an empirically derived number that varies over a range between 10 and 100 (the GSI is dimensionless), and can be estimated by examination of the quality of the rock-mass in situ—by direct inspection of an outcrop, for example. By definition, GSI values close to 10 correspond to very poor quality rock-masses, while GSI values close to 100 correspond to excellent quality rock-masses.

Figure A-3 (adapted from Hoek and Brown 1997, and Hoek et al. 1998) shows how the GSI can be estimated from the structure and surface conditions of the rock-mass (for example, a rock-mass with *Blocky / Disturbed* structure and *Poor* surface condition will have a GSI close to 30).

The value *GSI* = 25, indicated by a discontinuous line in Figure A-3, is significant in that it defines the limit between rock-masses of very poor quality (*GSI* < 25) and those of good to reasonable quality (*GSI* > 25). For rock-masses of good to reasonable quality (i.e., *GSI* > 25) the Geological Strength Index is equivalent to the *Rock Mass Rating (RMR)* introduced by Bieniawski (1976) when the rating for *Groundwater* is assessed as 'dry' and the rating for *Joint Orientation* as 'favorable'.

Table A-1. Reference values for the unconfined compressive strength σ_{ci}, Poisson's ratio n, Young's Modulus E, Shear Modulus G and unit weight γ for intact rock (adapted from Lama and Vutukuri 1978 and Goodman 1980).

Rock type	σ_{ci} [MPa]	ν	E [MPa]	G [MPa]	γ [MN/m^3]
1) Andesite	130.6	0.16	44.3×10^3	19.1×10^3	25.2×10^{-3}
2) Basalt	148.0	0.32	33.9×10^3	12.8×10^3	27.8×10^{-3}
3) Conglomerate	30.3	0.12	1.3×10^3	0.6×10^3	24.2×10^{-3}
4) Diabase	321.3	0.28	95.8×10^3	37.4×10^3	28.8×10^{-3}
5) Dolomite	46.9	0.29	29.0×10^3	11.2×10^3	24.5×10^{-3}
6) Gneiss	165.0	0.27	76.3×10^3	30.0×10^3	26.8×10^{-3}
7) Granite	141.1	0.22	73.8×10^3	30.3×10^3	26.4×10^{-3}
8) Limestone	51.0	0.29	28.5×10^3	11.1×10^3	23.3×10^{-3}
9) Quartzite	320.1	0.11	88.4×10^3	39.8×10^3	25.7×10^{-3}
10) Sandstone	73.8	0.38	18.3×10^3	6.6×10^3	21.4×10^{-3}
11) Siltstone	122.7	0.22	26.2×10^3	10.7×10^3	25.4×10^{-3}
12) Tuff	11.3	0.19	3.7×10^3	1.5×10^3	23.5×10^{-3}

Origin of the samples: *1)* Palisades Dam, Idaho, USA; *2)* Nevada Test Site, USA; *3)* Mc Dowell Dam, Arizona, USA; *4)* New York, USA; *5)* Minneapolis, Minnesota, USA; *6)* Graminha Dam, Brazil; *7)* Nevada Test Site, USA; *8)* Bedford, Indiana, USA; *9)* Baraboo, Wisconsin, USA; *10)* Amherst, Ohio, USA; *11)* Hackensack, N.Y., USA; *12)* Nevada Test Site, USA.

When the scaling factor GSI is introduced, the Hoek-Brown failure criterion for the *rock-mass* is given by the following relationship (Hoek and Brown 1997):

$$\sigma_1 = \sigma_3 + \sigma_{ci}\left(m_b \frac{\sigma_3}{\sigma_{ci}} + s\right)^a \qquad \text{(A-2)}$$

The parameter m_b in equation (A-2) depends on both the intact rock parameter m_i, of equation (A-1), and the value of GSI, as defined by the equation

$$m_b = m_i \exp\left(\frac{GSI - 100}{28}\right) \qquad \text{(A-3)}$$

The parameters s and a also depend empirically on the value of GSI as follows, for $GSI \geq 25$,

$$s = \exp\left(\frac{GSI - 100}{9}\right) \qquad \text{(A-4)}$$

$$a = 0.5$$

and for $GSI < 25$

$$s = 0 \qquad \text{(A-5)}$$

$$a = 0.65 - \left(\frac{GSI}{200}\right)$$

Table A-2 lists the values of m_b, s and a obtained from equations (A-3), (A-4) and (A-5) for different values of GSI. It can be seen that when GSI =100 (the hypothetical case in which the rock-mass has the same strength as the intact rock sample), the parameters are $m_b = m_i$, s =1 and a =0.5. With these values, the yield condition for the rock-mass, equation (A-2), and for the intact rock, equation (A-1), are the same.

Londe (1988) showed that the Hoek-Brown failure criterion defined by equation (A-2) can be transformed into a 'general' failure envelope that is independent of the parameters σ_{ci}, m_b and s.

The transformation suggested by Londe applies to the particular case a = 0.5 and involves dividing the stress magnitudes by $m_b \sigma_{ci}$ and adding the term s/m_b^2. Considering the parameters introduced in equation (A-2), the scaled stresses S_1 and S_3 can be defined as,

$$S_1 = \frac{\sigma_1}{m_b \sigma_{ci}} + \frac{s}{m_b^2} \qquad \text{(A-6)}$$

$$S_3 = \frac{\sigma_3}{m_b \sigma_{ci}} + \frac{s}{m_b^2} \qquad \text{(A-7)}$$

Rock type	Class	Group	Texture		
			Coarse	Medium	Fine
SEDIMENTARY	Clastic		Conglomerate (22)	Sandstone (19)	Siltstone (9)
	Non-clastic	Organic	..... Coal (8~21)		
		Carbonate	Breccia (20)	..... Limestone (8~10)	
METAMORPHIC	Non-foliated		Marble (9)	Hornfels (19)	Quartzite (24)
	Slightly foliated		Migmatite (30)	Amphibolite (25~31)	Mylonites (6)
	Foliated		Gneiss (33)	Schists (4~8)	Phyllites (10)
IGNEOUS	Light		Granite (33)		Rhyolite (16)
			Granodiorite (30)		Dacite (17)
	Dark		Gabbro (27)	Dolerite (19)	Basalt (17)
	Extrusive pyroclastic		Agglomerate (20)	Breccia (18)	Tuff (15)

Figure A-2. Reference values for the coefficient m_i for different rock types (adapted from Hoek and Brown 1997). The value of m_i is shown in parentheses below the name of the rock.

With the stresses σ_3 and σ_1 replaced by the scaled stresses S_3 and S_1 from equations (A-6) and (A-7), the failure criterion for the rock-mass, equation (A-2), can be written in the form (Londe 1988)

$$S_1 = S_3 + \sqrt{S_3} \qquad \text{(A-8)}$$

Note that in this 're-scaled' form of the failure criterion the parameters σ_{ci}, m_b and s are 'hidden' within the scaled stresses S_1 and S_3; the relationship applies then to any type of rock that is assumed to obey the Hoek-Brown criterion[b].

To illustrate the use of Londe's transformation, we will re-examine the triaxial test results for the samples of granite, quartz dolerite and marble presented in Figure A-1. Note that the results for intact rock samples can be equally approximated by equation (A-2), taking $GSI = 100$, $s = 1$, $m_b = m_i$ and $a = 0.5$. Figure A-4 represents the scattered pairs (σ_3, σ_1) of Figure A-1 together with the Hoek-Brown failure criterion—equation (A-2) or (A-1)—plotted in terms of scaled principal stresses (i.e., with the axes representing the transformed stresses S_1 and S_3 defined by equations A-6 and A-7). It is seen that the stresses at failure for all three types of rocks align now to the 'general' form of the Hoek-Brown criterion defined by equation (A-8).

The use of equation (A-8) rather than equation (A-2) can lead to important simplifications in mechanical analyses involving the Hoek-Brown criterion. Carranza-Torres and Fairhurst (1999) have applied the transformation (A-8) in solving the problem of excavating cylindrical and spherical openings in rock-masses that satisfy the Hoek-Brown failure criterion. This solution is the basis for construction of Ground Reaction Curves in the Convergence-Confinement method, discussed in Section 3.

Just as the strength of the rock-mass is usually lower than the strength of the intact rock, the (elastic) deformation modulus of the rock-mass is also usually lower than that of the intact rock. Serafim and Pereira (1983) have proposed an empirical relationship to compute the deforma-

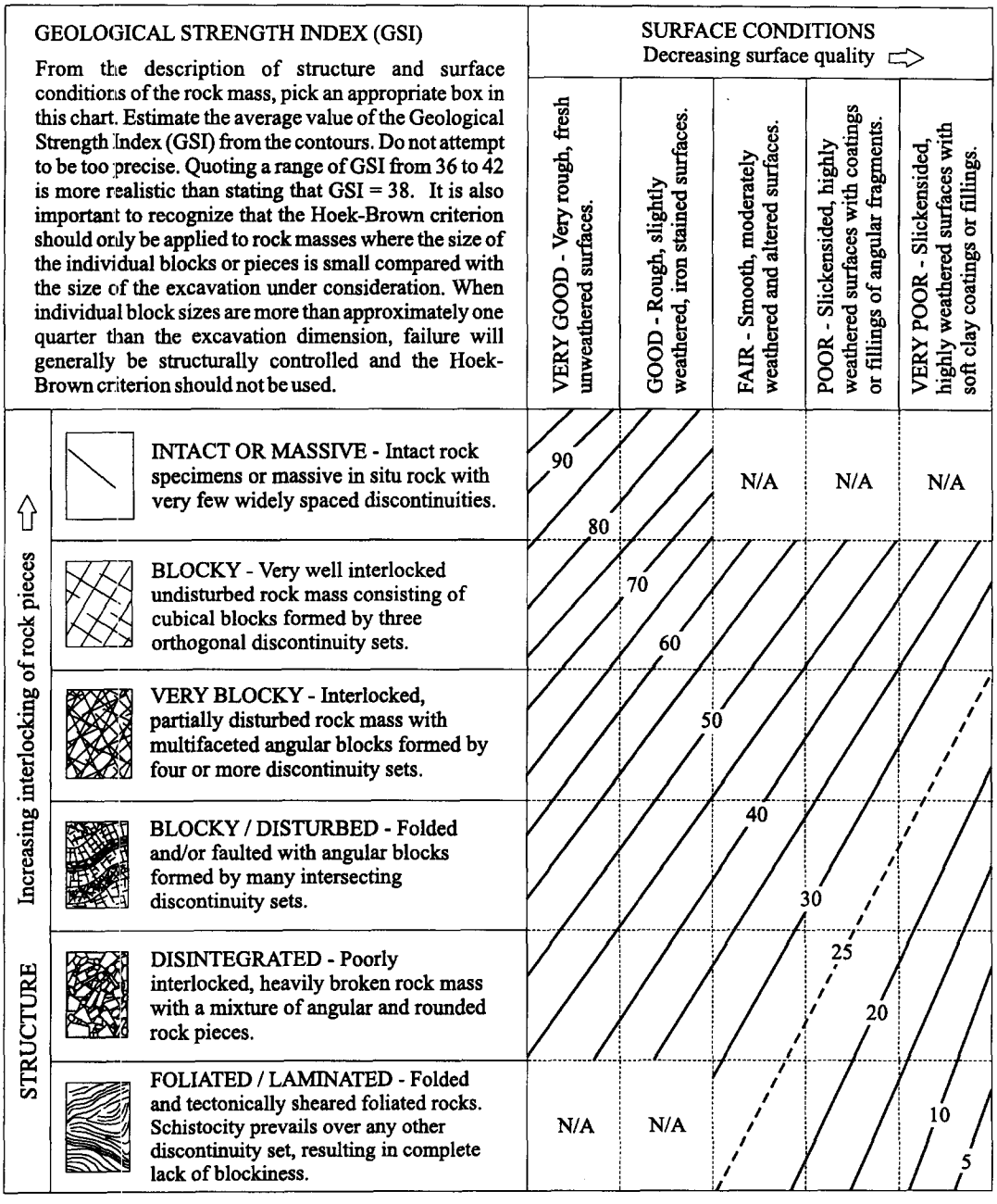

Figure A-3. Empirical chart for the estimation of the Geological Strength Index (GSI) based on the characteristics of the rock-mass (adapted from Hoek and Brown 1997 and Hoek et al. 1998).

Table A-2. Values of coefficients m_b, s and a as a function of the Geological Strength Index (GSI), computed from equations (A-3), (A-4) and (A-5), respectively. (Note that the second column represents ratio m_b/m_i; values of m_i for different rock types are given in Figure A-2).

GSI	m_b/m_i	s	a
100	1.00	1.00	0.5
75	40.95×10^{-2}	621.77×10^{-4}	0.50
50	16.77×10^{-2}	38.66×10^{-4}	0.50
25^+	6.87×10^{-2}	2.40×10^{-4}	0.50
25^-	6.87×10^{-2}	0.00	0.53
10	4.02×10^{-2}	0.00	0.60

tion modulus of the rock-mass from the unconfined compressive strength of the intact rock sample and the value of the Rock Mass Rating (RMR) by Bienawski (1976). Based on the original equation by Serafim and Pereira, Hoek and Brown (1997) propose the following relationship between the rock-mass modulus E_{rm} and the Geological Strength Index *GSI*:

$$E_{rm} = 1000\, C(\sigma_{ci})\, 10^{\frac{GSI-10}{40}} \qquad \text{(A-9)}$$

where

$$C(\sigma_{ci}) = 1 \quad \text{if } \sigma_{ci} \geq 100 \text{ MPa}$$
$$= \sqrt{\frac{\sigma_{ci}}{100}} \quad \text{if } \sigma_{ci} \leq 100 \text{ MPa}$$

In equation (A-9), both the unconfined compressive strength σ_{ci} and the rock-mass modulus E_{rm} are expressed in MPa.

In elasto-plastic analyses of deformations—such as the one presented later in Section 3, the rock-mass shear modulus G_{rm} is used rather than the deformation modulus E_{rm} given by equation (A-9). The shear modulus of the rock-mass can be estimated from the deformation modulus using the classic relationship from isotropic elasticity,

$$G_{rm} = \frac{E_{rm}}{2(1+\upsilon)} \qquad \text{(A-10)}$$

In equation (A-10), ν is Poisson's ratio for the rock-mass, and is usually considered to vary between 0.1 and 0.3 (Hoek and Brown 1980).

To illustrate the application of equations (A-9) and (A-10), let us consider the properties of the granite sample listed in Table A-1. The unconfined compressive strength of the intact rock is approximately σ_{ci} = 141 MPa; if the Geological Strength Index of the rock-mass is *GSI* = 50, then the deformation modulus of the rock-mass is, from equation (A-9), E_{rm} = 1187 MPa. If Poisson's ratio for the intact rock and rock-mass are both assumed to be equal to 0.22 then, from equation (A10), the shear modulus of the rock-mass is

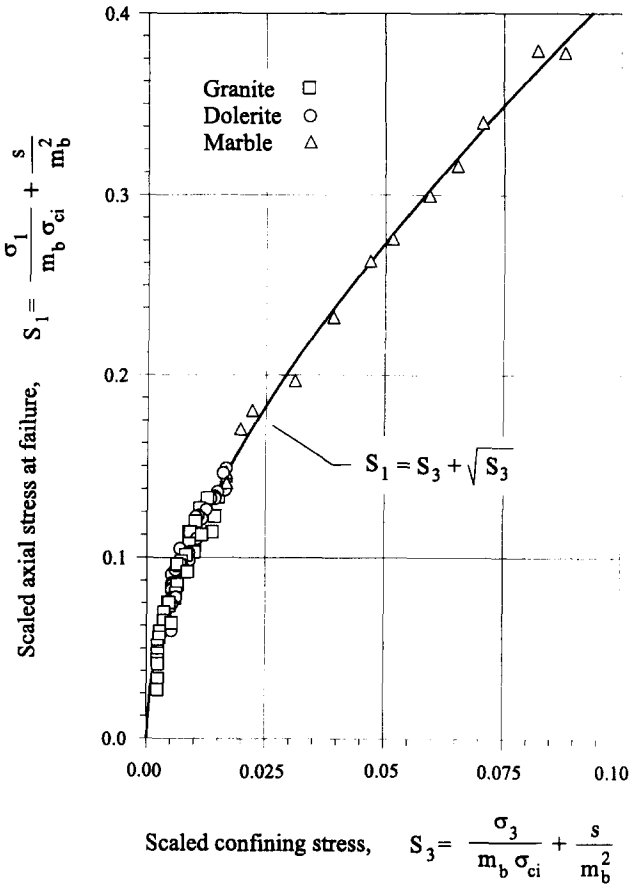

Figure A-4. Results from triaxial tests shown in Figure A-1 with the principal stress axes σ_1 and σ_3 normalized according to transformations (A-6) and (A-7). Note that in this reference system results for all three rock types fall on the 'general' failure envelope given by equation (A-8) (Londe 1988).

G_{rm}=486 MPa. The elastic constants E_{rm} and G_{rm} for the rock-mass are seen to be significantly lower than the corresponding constants E and G for the intact rock sample listed in Table A-1.

Notes for Appendix A

a) The observed dispersion appears to be proportional to the number of specimens tested, with the highest dispersion for the 48 samples of granite and the lowest for the 14 samples of marble (see Appendix B).

b) It should be emphasized though that the equation (A-8) is strictly valid only when the parameter a in equation (A-2) is equal to 0.5. According to equations (A-4) and (A-5), a = 0.5 for the broad range of situations in which *GSI* = 25.

Appendix B. Determination of the parameters σ_{ci} and m_i from results of triaxial tests on intact rock samples.

The parameters σ_{ci} and m_i in equation (A-1) can be obtained from statistical analysis of the (σ_3, σ_1) results obtained from triaxial tests on intact rock specimens —σ_3 is the constant confining stress applied to the sample and σ_1 is the axial stress that produces collapse of the sample. Hoek (1983) describes the basis of the statistical analysis and the needed equations. A brief summary of the equations is presented below.

If n rock cores have been tested and n pairs (σ_3, σ_1) have been obtained from the tests, the parameters σ_{ci} and m_i can be found from the following expressions (Hoek 1983):

$$\sigma_{ci}^2 = \frac{\Sigma(\sigma_1-\sigma_3)^2}{n} - \frac{\Sigma\sigma_3}{n}\left[\frac{n\,\Sigma\sigma_3(\sigma_1-\sigma_3)^2 - \Sigma\sigma_3\,\Sigma(\sigma_1-\sigma_3)^2}{n\,\Sigma\sigma_3^2-(\Sigma\sigma_3)^2}\right] \quad \text{(B-1)}$$

$$m_i = \frac{1}{\sigma_{ci}}\left[\frac{n\,\Sigma\sigma_3(\sigma_1-\sigma_3)^2 - \Sigma\sigma_3\,\Sigma(\sigma_1-\sigma_3)^2}{n\,\Sigma\sigma_3^2-(\Sigma\sigma_3)^2}\right] \quad \text{(B-2)}$$

A regression coefficient r can be evaluated to estimate the 'goodness of fit' of the parabolic approximation. The coefficient is computed as,

$$r^2 = \frac{\left[n\,\Sigma\sigma_3(\sigma_1-\sigma_3)^2 - \Sigma\sigma_3\,\Sigma(\sigma_1-\sigma_3)^2\right]^2}{\left[n\,\Sigma\sigma_3^2-(\Sigma\sigma_3)^2\right]\left[n\,\Sigma(\sigma_1-\sigma_3)^4-\left(\Sigma(\sigma_1-\sigma_3)^2\right)^2\right]} \quad \text{(B-3)}$$

For example, Table B-1 lists the pairs (σ_3, σ_1) obtained by Franklin and Hoek (1970) from triaxial tests on samples of granite, quartz dolerite and marble —these results have been discussed in Appendix A (see Fig. A-1).

The parameters σ_{ci}, m_i and r^2 computed using the equations B-1, B-2 and B-3 are indicated below the values of σ_3 and σ_1 for each rock type.

Table B-1. Stress pairs (σ_3, σ_1) obtained from triaxial tests on different rock samples (after Franklin and Hoek 1970). The parameters σ_{ci}, m_i and r^2, obtained with equations (B-1) through (B-3) are indicated below the tabulated (σ_3, σ_1) values.

Granite (48 samples from Blackingstone quarry, Devon, UK)

σ_3 [MPa]	σ_1 [MPa]	σ_3 [MPa]	σ_1 [MPa]	σ_3 [MPa]	σ_1 [MPa]
9.3	309.3	43.5	541.0	29.4	485.8
43.2	539.8	0.0	179.3	12.8	269.9
55.8	569.5	0.0	111.3	49.3	488.4
2.8	249.0	1.6	234.3	18.0	410.7
0.0	197.3	19.7	406.5	0.0	195.9
21.4	407.6	0.0	201.5	28.8	458.0
10.7	316.0	25.8	431.1	0.0	196.1
34.8	512.7	0.0	193.4	5.3	270.5
0.0	171.5	38.1	543.7	21.7	415.9
6.5	273.3	22.9	409.9	33.0	440.1
0.0	135.9	27.1	392.8	16.4	340.4
5.0	293.1	13.2	359.0	8.7	318.5
7.8	276.8	28.5	486.8	9.9	312.1
33.9	453.9	7.8	283.0	45.5	566.0
0.0	213.6	39.2	480.8	7.4	284.4
51.7	523.9	15.1	330.1	17.7	362.3

$\sigma_{ci} = 210$ MPa; $m_i = 21$; $r^2 = 0.91$

Quartz Dolerite (38 samples from Northumberland, UK)

σ_3 [MPa]	σ_1 [MPa]	σ_3 [MPa]	σ_1 [MPa]	σ_3 [MPa]	σ_1 [MPa]
5.0	333.8	44.1	561.2	0.0	331.8
0.0	315.0	34.7	498.9	7.4	344.6
23.9	453.6	20.2	410.9	3.5	284.7
0.0	311.4	0.0	305.1	0.0	267.5
0.0	314.4	10.3	341.9	0.0	299.7
6.9	390.5	34.5	497.8	27.6	489.0
20.7	457.1	0.0	272.9	2.4	341.0
1.3	328.3	42.9	514.8	37.0	512.7
0.0	315.7	13.7	380.7	0.0	214.4
28.3	474.6	0.0	210.7	13.9	364.0
31.0	496.4	0.0	275.8	0.0	273.7
17.2	422.6	0.0	312.0	0.0	278.9
42.1	552.2	21.7	461.2		

$\sigma_{ci} = 294$ MPa; $m_i = 13$; $r^2 = 0.92$

Carrara Marble (14 samples from Italy)

σ_3 [MPa]	σ_1 [MPa]	σ_3 [MPa]	σ_1 [MPa]	σ_3 [MPa]	σ_1 [MPa]
30.9	205.9	0.0	90.3	35.2	217.2
3.9	119.1	39.1	234.4	51.7	262.2
0.0	93.1	21.8	179.2	25.2	188.1
16.2	156.4	10.5	131.1	0.0	93.8
2.2	111.6	47.5	263.1		

$\sigma_{ci} = 94$ MPa; $m_i = 8$; $r^2 = 0.99$

Appendix C. Spreadsheet implementation of the Convergence-Confinement method.

Figures C-1 through C-3 present a computer spreadsheet for implementation of equations in Sections 3, 4 and 5, in order to construct the GRC, SCC and LDP curves, respectively.

The spreadsheet is divided in two main parts: *a)* Input of data and *b)* Output of results.

In part *a)* (Fig. C-1), the geometry, rock-mass properties, loading conditions, distance to the face and properties of the three support systems discussed in Section 4 are entered.

In part *b)* (Figs. C-2 and C-3), the elastic and plastic parts of the GRC, the LDP (from equation 18) and the SCC for individual and combined supports are defined.

Linking of the cells in the spreadsheet is accomplished by giving a name to each cell and range of cells, and expressing formulae within the spreadsheet in terms of the named cells (see for example, Dodge et al. 1997).

The names given to *individual* cells are indicated within parentheses at the side of the cells in Figures C-1 through C-3.

For *ranges* of cells, defined by a box outlined by dashed lines, the name is indicated at the bottom of the box.

The values in the shaded cells in the spreadsheet are computed with formulas.

Tables C-1 and C-2 define the formulas for Figures C-2 and C-3—expressed in terms of cell/range names—that need to be entered in these cells.

Note that the values shown in the spreadsheet are those for the practical example discussed in Section 6. To construct the different curves shown in the diagram of Figure 10, the following ranges must be plotted:

- for the GRC, the ranges ure_grc and urp_grc in the horizontal axis and the ranges pip_grc, pip_grc, pip_r_grc and pip_f_grc in the vertical axis; the last two ranges correspond to the internal pressure at the crown and floor of the tunnel—see points C and F in Figure 10a.
- for the LDP, the range ur_ldp in the horizontal axis and the range lf in the vertical axis.
- for the SCC of individual supports, the ranges ur_sc, ur_ss and ur_sb in the horizontal axis and the ranges pi_sc, pi_ss and pi_sb in the vertical axis.
- for the SCC of combined supports, the ranges ur_sc_b, and ur_ss_b in the horizontal axis and the ranges pi_sc_b and pi_ss_b in the vertical axis.

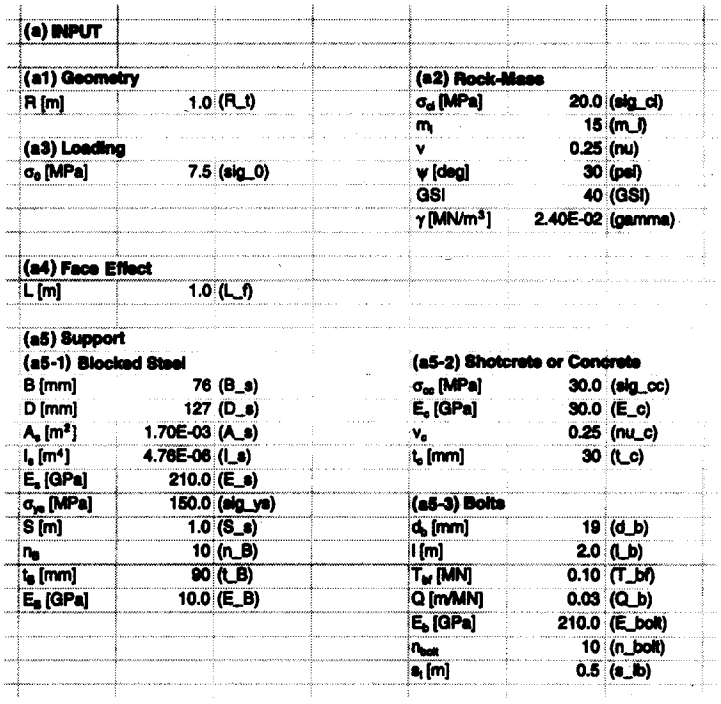

(a) INPUT					
(a1) Geometry			(a2) Rock-Mass		
R [m]	1.0	(R_t)	σ_{cl} [MPa]	20.0	(sig_cl)
			m_i	15	(m_i)
(a3) Loading			ν	0.25	(nu)
σ_0 [MPa]	7.5	(sig_0)	ψ [deg]	30	(psi)
			GSI	40	(GSI)
			γ [MN/m^3]	2.40E-02	(gamma)
(a4) Face Effect					
L [m]	1.0	(L_f)			
(a5) Support					
(a5-1) Blocked Steel			(a5-2) Shotcrete or Concrete		
B [mm]	76	(B_s)	σ_{cc} [MPa]	30.0	(sig_cc)
D [mm]	127	(D_s)	E_c [GPa]	30.0	(E_c)
A_s [m^2]	1.70E-03	(A_s)	ν_c	0.25	(nu_c)
I_s [m^4]	4.76E-06	(I_s)	t_c [mm]	30	(t_c)
E_s [GPa]	210.0	(E_s)			
σ_{ys} [MPa]	150.0	(sig_ys)	(a5-3) Bolts		
S [m]	1.0	(S_s)	d_b [mm]	19	(d_b)
n_B	10	(n_B)	l [m]	2.0	(l_b)
t_B [mm]	90	(t_B)	T_{bf} [MN]	0.10	(T_bf)
E_B [GPa]	10.0	(E_B)	Q [m/MN]	0.03	(Q_b)
			E_b [GPa]	210.0	(E_bolt)
			n_{bolt}	10	(n_bolt)
			s_l [m]	0.5	(s_lb)

Figure C-1. First page of the spreadsheet. Data input.

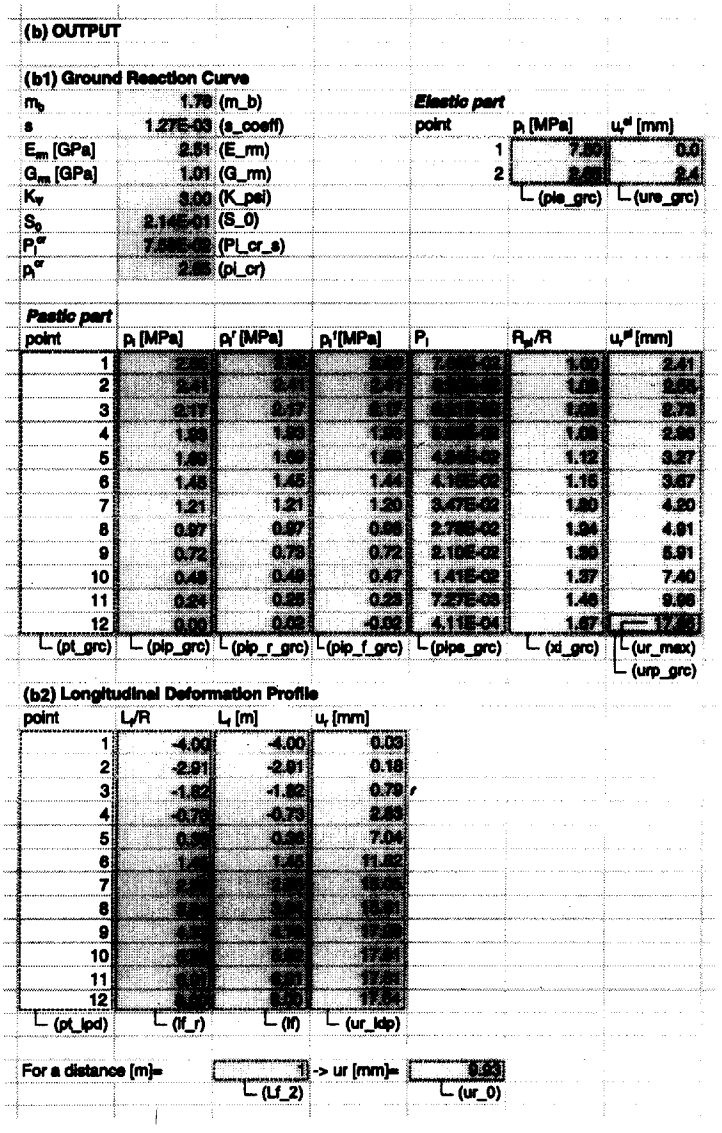

(b) OUTPUT

(b1) Ground Reaction Curve

m_b	1.70	(m_b)
s	1.27E-03	(s_coeff)
E_m [GPa]	2.51	(E_rm)
G_m [GPa]	1.01	(G_rm)
K_ψ	3.00	(K_psi)
S_0	2.14E-01	(S_0)
P_i^{cr}	7.68E-02	(Pi_cr_s)
p_i^{cr}	2.88	(pi_cr)

Elastic part

point	p_i [MPa]	u_i^{el} [mm]
1	7.50	0.0
2	2.88	2.4
	(pie_grc)	(ure_grc)

Plastic part

point	p_i [MPa]	p_i' [MPa]	p_i''[MPa]	P_i	R_{pl}/R	u_i^{pl} [mm]
1	2.88	2.88	2.88	7.23E-02	1.00	2.41
2	2.81	2.81	2.81	6.93E-02	1.02	2.65
3	2.77	2.77	2.77	6.80E-02	1.03	2.75
4	1.69	1.69	1.69	3.97E-02	1.08	2.98
5	1.49	1.49	1.49	4.24E-02	1.12	3.27
6	1.45	1.45	1.44	4.10E-02	1.15	3.67
7	1.21	1.21	1.20	3.47E-02	1.20	4.20
8	0.97	0.97	0.96	2.76E-02	1.24	4.81
9	0.72	0.73	0.72	2.10E-02	1.29	5.51
10	0.48	0.49	0.47	1.41E-02	1.37	7.40
11	0.24	0.25	0.23	7.27E-03	1.46	9.66
12	0.00	0.02	-0.02	4.11E-04	1.67	17.86
	(pt_grc)	(pip_grc)	(pip_r_grc)	(pip_f_grc)	(pipe_grc)	(xi_grc)

(ur_max)
(urp_grc)

(b2) Longitudinal Deformation Profile

point	L_i/R	L_i [m]	u_i [mm]
1	-4.00	-4.00	0.03
2	-2.91	-2.91	0.18
3	-1.82	-1.82	0.79
4	-0.73	-0.73	2.83
5	0.36	0.36	7.04
6	1.45	1.45	11.82
7	2.54	2.54	15.56
8	3.63	3.63	16.91
9	4.72	4.72	17.39
10	5.81	5.81	17.61
11	6.91	6.91	17.84
12	8.00	8.00	17.94
	(pt_ldp)	(lf_r)	(lf)	(ur_ldp)

For a distance [m]= 1 (Lf_2) -> ur [mm]= 0.03 (ur_0)

Figure C-2 (at left). Second page of the spreadsheet. Computation of the GRC and LDP.

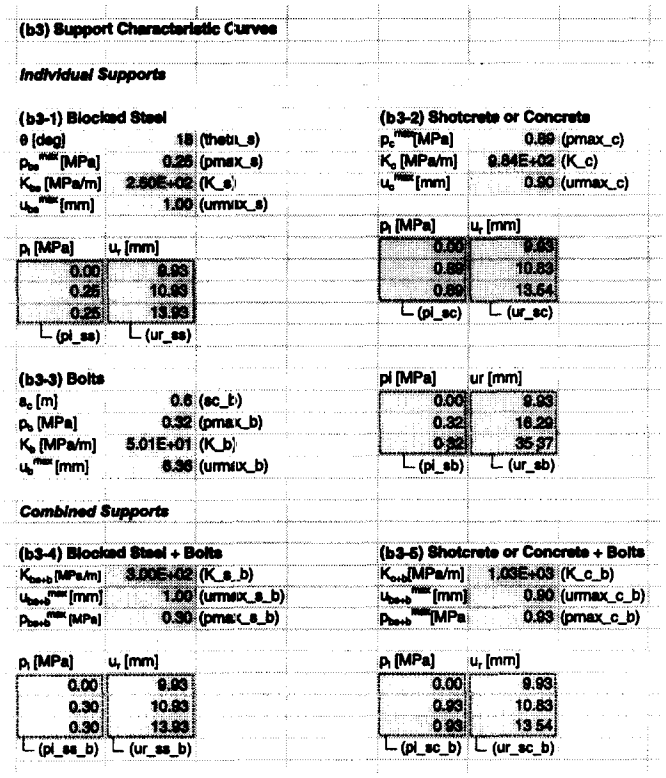

Figure C-3. Third page of the spreadsheet. Computation of the SCC.

Table C-1. Formulas to be entered in the shaded cells in Figure 2.

m_b =m_i*EXP((GSI-100)/28)
s_coeff =IF(GSI>=25,EXP((GSI-100)/9),0)
E_rm =SQRT(sig_ci/100)*10^((GSI-10)/40)
G_rm =E_rm/2/(1+nu)
K_psi =(1+SIN(psi*PI()/180))/(1-SIN(psi*PI()/180))
S_0 =sig_0/(m_b*sig_ci)+s_coeff/m_b^2
Pi_cr_s =1/16*(1-SQRT(1+16*S_0))^2
pi_cr =(Pi_cr_s-s_coeff/(m_b^2))*m_b*sig_ci
pie_grc =sig_0 (first row), =pi_cr (second row)
ure_grc =(sig_0-pie_grc)/2/(G_rm*1000)*R_t*1000
pip_grc =pi_cr*(12-pt_grc)/11
pip_r_grc =pip_grc+gamma*(xi_grc*R_t-R_t)
pip_f_grc =pip_grc-gamma*(xi_grc*R_t-R_t)
pips_grc =pip_grc/(m_b*sig_ci)+s_coeff/m_b^2
xi_grc =EXP(2*(SQRT(Pi_cr_s)-SQRT(pips_grc)))
urp_grc =((K_psi-1)/(K_psi+1)+2/(K_psi+1)*xi_grc
^(K_psi+1)+(1-2*nu)/4/(S_0-Pi_cr_s)*LN(xi_grc)^2
-((1-2*nu)/(K_psi+1)*(SQRT(Pi_cr_s))/(S_0-Pi_cr_s)
+(1-nu)/2*(K_psi-1)/(K_psi+1)^2/(S_0-Pi_cr_s))
*((K_psi+1)*LN(xi_grc)-(xi_grc)^(K_psi+1)+1))
R_t(sig_0-pi_cr)/2/(G_rm*1000)*1000
lf_r =-4+(pt_ldp-1)*12/11
lf =lf_r*R_t
ur_ldp =ur_max*(1+EXP(-lf/1.1/R_t))^-1.7
Lf_2 =L_f
ur_0 =ur_max*(1+EXP(-L_f/1.1/R_t))^-1.7

Table C-2. Formulas to be entered in the shaded cells in Figure C-3.

theta_s =180/n_B
pmax_s =(3*A_s*I_s*sig_ys)/(2*S_s*R_t*theta_s*PI()/180
*(3*I_s+D_s/1000*A_s*(R_t-t_B/1000-0.5*D_s/1000)
*(1-COS(theta_s*PI()/180))))
K_s =1/(((S_s*R_t^2)/(E_s*1000*A_s))+(S_s*R_t^4/(E_s*1000*I_s)
*((theta_s*PI()/180*(theta_s*PI()/180+SIN(theta_s*PI()
/180)*COS(theta_s*PI()/180)))/(2*(SIN(theta_s*PI()/180)
^2))-1)+(2*S_s*theta_s*PI()/180*t_B/1000*R_t)/(E_B*1000
*(B_s/1000)^2))
urmax_s =pmax_s/K_s*1000
pi_ss =0 (first row), =pmax_s (second and third rows)
ur_ss =ur_0 (first row), =ur_0+urmax_s (second row)
=ur_0+urmax_s*4 (third row)
pmax_c =sig_cc/2*(1-(R_t-t_c/1000)^2/R_t^2)
K_c =E_c*1000/(1+nu_c)*(R_t^2-(R_t-t_c/1000)^2)/((1-2*nu_c)*
R_t^2+(R_t-(t_c/1000))^2)/R_t
urmax_c =pmax_c/K_c*1000
pi_sc =0 (first row), =pmax_c (second and third rows)
ur_sc =ur_0 (first row), =ur_0+urmax_c (second row)
=ur_0+urmax_c*4 (third row)
sc_b =2*PI()*R_t/n_bolt
pmax_b =T_bf/sc_b/s_lb
K_b =1/(sc_b*s_lb)*(PI()*(d_b/1000)^2*E_bolt*1000)/(4*l_b+
Q_b*PI()*(d_b/1000)^2*E_bolt*1000)
urmax_b =pmax_b/K_b*1000
pi_sb =0 (first row), =pmax_b (second and third rows)
ur_sb =ur_0 (first row), =ur_0+urmax_b (second row)
=ur_0+urmax_b*4 (third row)
K_s_b =K_s+K_b
urmax_s_b =IF(urmax_s<urmax_b,urmax_s,urmax_b)
pmax_s_b =K_s_b*urmax_s_b/1000
pi_ss_b =0 (first row), =pmax_s_b (second and third rows)
ur_ss_b =ur_0 (first row), =ur_0+urmax_s_b (second row)
=ur_0+urmax_s_b*4 (third row)
K_c_b =K_c+K_b
urmax_c_b =IF(urmax_c<urmax_b,urmax_c,urmax_b)
pmax_c_b =K_c_b*urmax_c_b/1000
pi_sc_b =0 (first row), =pmax_c_b (second and third rows)
ur_sc_b =ur_0 (first row), =ur_0+urmax_c_b (second row)
=ur_0+urmax_c_b*4 (third row)

Appendix D. Elastic analysis of circular tunnels in non-uniform stress conditions.

The elastic solution of a circular cavity of radius R subject to non-uniform horizontal and vertical far-field stresses σ_x and σ_z, respectively, and internal pressure p_i is given by the classical Kirsch solution (see, for example, Timoshenko and Goodier 1970).

Considering the mean stress σ_o and the horizontal-to-vertical stress coefficient k defined by equations (21) and (20), respectively, the scaled radial stress σ_r/σ_o at a distance r from the center of the cavity is given by,

$$\frac{\sigma_r(r)}{\sigma_o} = 1 - \left(\frac{R}{r}\right)^2 + \frac{k-1}{k+1}\left[1 - 4\left(\frac{R}{r}\right)^2 + 3\left(\frac{R}{r}\right)^4\right]\cos(2\theta) + \frac{p_i}{\sigma_o}\left(\frac{R}{r}\right)^2 \qquad \text{(D-1)}$$

The scaled 'hoop' stress σ_θ/σ_o is

$$\frac{\sigma_\theta(r)}{\sigma_o} = 1 + \left(\frac{R}{r}\right)^2 - \frac{k-1}{k+1}\left[1 + 3\left(\frac{R}{r}\right)^4\right]\cos(2\theta) - \frac{p_i}{\sigma_o}\left(\frac{R}{r}\right)^2 \qquad \text{(D-2)}$$

and the scaled shear stress $\sigma_{r\theta}/\sigma_o$ is

$$\frac{\sigma_{r\theta}(r)}{\sigma_o} = -\frac{k-1}{k+1}\left[1 + 2\left(\frac{R}{r}\right)^2 - 3\left(\frac{R}{r}\right)^4\right]\sin(2\theta) \qquad \text{(D-3)}$$

The maximum and minimum principal stresses —σ_1 and σ_3, respectively, corresponding to the stresses σ_r, σ_θ and $\sigma_{r\theta}$ defined above—are computed using the classic relationships (see, for example, Jaeger and Cook 1979):

$$\sigma_3^1(r)/\sigma_o = \frac{\sigma_\theta/\sigma_o + \sigma_r/\sigma_o}{2} \pm \sqrt{\left(\frac{\sigma_\theta/\sigma_o - \sigma_r/\sigma_o}{2}\right)^2 - (\sigma_{r\theta}/\sigma_o)^2} \qquad \text{(D-4)}$$

The extent r of the 'over-stressed' region discussed in Section 7 can be found from the condition that the strength of the material —defined by the Hoek-Brown failure criterion (A-2)— is exceeded. Considering the parameter a to have the value 0.5 in equation (A-2), the condition is written as,

$$\sigma_1(r) \geq \sigma_3(r) + \sigma_{ci}\left(m_b\,\frac{\sigma_3(r)}{\sigma_{ci}} + s\right)^a \qquad \text{(D-5)}$$

The maximum value of r, can be obtained from the condition that the left and right sides of expression (D-5) are equal. Thus, dividing both sides by $m_b\,\sigma_{ci}$ and multiplying and dividing each term by σ_o, the inequality (D-5) transforms into

$$\frac{\sigma_1(r)/\sigma_o}{m_b\,\sigma_{ci}/\sigma_o} = \frac{\sigma_3(r)/\sigma_o}{m_b\,\sigma_{ci}/\sigma_o} + \sqrt{\frac{\sigma_3(r)/\sigma_o}{m_b\,\sigma_{ci}/\sigma_o} + \frac{s}{m_b^2}} \qquad \text{(D-6)}$$

The non-linear equation (D-6) must be solved for the unknown r. Because of the method of scaling used in equation (D-6), the values obtained for the extent r are valid for constant ratios of $m_b\,\sigma_{ci}/\sigma_o$ and $s\,/\,m_b^2$ (see example in Fig. 13).

(A) INPUT

(A1) Geometry			**(A2) Rock mass properties**		
R [m]	1.0	(R_t)	σ_{ci} [MPa]	20.0	(sig_ci)
			m_i	15	(m_i)
(A3) Loading			GSI	40	(GSI)
σ_x [MPa]	4.65	(sx)	v	0.25	(nu)
σ_z [MPa]	10.34	(sz)			
p_i [MPa]	0.00	(pi)			

(B) OUTPUT

σ_o [MPa]	7.50	(s0)	m_b	1.76	(m_b)
k	0.45	(k)	s	1.27E-03	(s_coeff)
p_i/σ_o	0.00	(pi_s0)	E_m [GPa]	2.51	(E_rm)
σ_{ci}/σ_o	2.67	(sci_s0)	G_m [GPa]	1.01	(G_rm)

point	θ [deg]	σ_r/σ_o	σ_θ/σ_o	$\sigma_{r\theta}/\sigma_o$	σ_1	σ_3	Condit.	r/R
1	-90.0	0.07	0.86	0.00	0.86	0.07	0.00	1.10
2	-78.8	0.12	0.79	-0.11	0.81	0.10	0.00	1.14
3	-67.5	0.29	1.04	-0.29	1.14	0.19	0.00	1.27
4	-56.3	0.49	1.23	-0.45	1.44	0.28	0.00	1.45
5	-45.0	0.59	1.41	-0.50	1.65	0.35	0.00	1.58
6	-33.8	0.59	1.66	-0.46	1.83	0.42	0.00	1.52
7	-22.5	0.58	1.95	-0.34	2.03	0.50	0.00	1.43
8	-11.3	0.58	2.15	-0.18	2.17	0.56	0.00	1.39
9	0.0	0.58	2.22	0.00	2.22	0.56	0.00	1.38
10	11.3	0.58	2.15	0.18	2.17	0.56	0.00	1.39
11	22.5	0.58	1.95	0.34	2.03	0.50	0.00	1.43
12	33.8	0.59	1.66	0.46	1.83	0.42	0.00	1.52
13	45.0	0.59	1.41	0.50	1.65	0.35	0.00	1.58
14	56.3	0.49	1.23	0.45	1.44	0.28	0.00	1.45
15	67.5	0.29	1.04	0.29	1.14	0.19	0.00	1.27
16	78.8	0.12	0.79	0.11	0.81	0.10	0.00	1.14
17	90.0	0.07	0.86	0.00	0.86	0.07	0.00	1.10
(point)	(theta)	(sr_s0)	(st_s0)	(srt_s0)	(s_1)	(s_3)	(yield)	(r_R)

Figure D-1. Spreadsheet for evaluation of the extent of the 'over-stressed' region around a circular cavity subject to uniform internal pressure and unequal far-field principal stresses.

The solution of the non-linear equation (D-6) can be found with a spreadsheet such as shown in Figure D-1. Linkage between cells in the spreadsheet is accomplished using the formulae listed in Table D-1. Note that, as in the spreadsheet presented in Appendix C, cell and range-of-cell names are indicated within parentheses in Figure D-1.

The equation solver implemented in most spreadsheet packages has to be used to evaluate the cells in the range r_R. In the commercial spreadsheet program *Excel* (see for example, Dodge et al. 1997) the 'Goal seek' tool has to be applied specifying *'Set cell:'* to point to cells in the range yield, *'To value:'* to be equal to 0.0 and *'By changing cell:'* to point to the cells in the range r_R. Note that in this spreadsheet program, the 'Goal seek' tool applies to individual cells, so that a macro should be recorded in order to find the solution in all cells of the range r_R simultaneously.

Diagrams such as those presented in Figure 13a can then be constructed by plotting the ranges theta and r_R in radial coordinates.

Table D-1. Formulae to be entered in the shaded cells of the spreadsheet shown in Figure D-1.

s0 =0.5*(sx+sz)
k =sx/sz
pi_s0 =pi/s0
sci_s0 =sig_ci/s0
m_b =m_i*EXP((GSI-100)/28)
s_coeff =IF(GSI>=25,EXP((GSI-100)/9),0)
E_rm =SQRT(sig_ci/100)*10^((GSI-10)/40)
G_rm =E_rm/2/(1+nu)

theta =-90+180*(point-1)/16
sr_s0 =1-1/r_R^2+(k-1)/(k+1)*(1-4*1/r_R^2+3*1/r_R^4)
*COS(2*theta*PI()/180)+pi_s0*1/r_R^2
st_s0 =1+1/r_R^2-(k-1)/(k+1)*(1+3*1/r_R^4)
*COS(2*theta*PI()/180)-pi_s0*1/r_R^2
srt_s0 =-(k-1)/(k+1)*(1+2*1/r_R^2-3*1/r_R^4)
*SIN(2*theta*PI()/180)
s_1 =(sr_s0+st_s0)/2+SQRT((sr_s0-st_s0)^2/4+srt_s0^2)
s_3 =(sr_s0+st_s0)/2-SQRT((sr_s0-st_s0)^2/4+srt_s0^2)
yield =s_1/(m_b*sci_s0)-s_3/(m_b*sci_s0)
-SQRT(s_3/(m_b*sci_s0)+s_coeff/m_b^2)
r_R (see main text)